Earth Energy Science 1 (2025) 306–323

Contents lists available at ScienceDirect

Earth Energy Science

journal homepage: www.keaipublishing.com/en/journals/earth-energy-science/

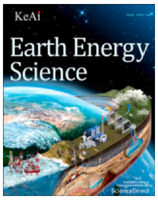

A parameter study of how initial roughness and normal stress affect the flow and transport properties in granitic-like sheared synthetic fractures

Martin Stigsson[a,*], Vladimir Cvetkovic[b], Diego Mas Ivars[a,c], Jan-Olof Selroos[a,b]

[a] SKB, Swedish Nuclear Fuel and Waste Management Co, PO Box 3091, Solna SE-169 03, Sweden
[b] KTH, Royal Institute of Technology, Sustainable development, Environmental science and Engineering (SEED), Teknikringen 10 B, Stockholm SE-100 44, Sweden
[c] KTH, Royal Institute of Technology, Civil and Architectural Engineering, Brinellvägen 23, Stockholm SE-10044, Sweden

ARTICLE INFO

Keywords:
Aperture distribution
Flow
Fractal
Normal stress
Roughness
Self-affine
Shearing
Transport properties

ABSTRACT

Flow and transport properties of fractured crystalline rock are of great interest for different geotechnical applications, such as storage of carbon dioxide, extraction of geothermal energy, or geologic storage of hazardous waste. For the long-term safety assessment of geological storage of hazardous waste, the understanding of flow and transport properties through the network of fractures is essential. The flow and transport behaviour can be explored using numerical models to investigate what parameters that affect the results. In this work a pilot study is carried out for multiple realizations of single realistic fractures, using fractal theories, which then are numerically sheared using a semi-analytical algorithm. The aperture field is calculated using the average distance of the volume integral of the void that a 1 mm lateral displacement of the sheared surfaces generates. The flow field through the aperture field is solved using Reynolds lubrication equation in linear triangular finite elements. The transport properties, travel length, travel time, transport resistance and specific flow wetted surface, are calculated in a Lagrangian framework using 10,000 particles for each of the 128 flow fields. Evaluating these four metrics, varying initial roughness, $4 < \text{JRC} < 10$ and normal stress between 0.2 and 20 MPa during shearing, it is concluded that an increase in normal stress generally results in longer travel paths, longer travel times, higher transport resistance and larger specific flow wetted surface while an increase of initial roughness will generally result in longer travel paths, shorter travel times, lower transport resistance and smaller specific flow wetted surface.

1. Introduction

Flow and transport properties of fractured crystalline rock are of great interest for different geotechnical applications. Typically, such applications include storage of carbon dioxide; extraction of geothermal energy; or geologic storage of hazardous waste such as mercury or radioactive waste (Neuman, 2005). For the long-term safety assessment of geological storage of hazardous waste, the understanding of flow and transport properties through the network of fractures is essential (Tsang et al., 2015). Fracture networks in real rock masses, are made up of many single fractures and, hence, the understanding of the flow and transport behaviour through the single fractures is the foundation for understanding the flow and transport through the network of fractures (Cvetkovic and Frampton, 2010; Blessent et al., 2011; Maillot et al., 2016).

There are different approaches to numerically calculate the flow and transport through a fracture. A simple and widespread approach is to assume that a fracture is the void between two parallel plates where the transmissivity is calculated using the cubic law (Witherspoon et al., 1980; Zimmerman and Bodvarsson, 1996). Such simplifications may be good enough for the calculation of bulk flow through the fracture and may describe some channelling effects through a network of fractures (Maillot et al., 2016, Hyman, 2020). However, it will neglect the internal aperture heterogeneity distribution and hence overlook the fact that flow will follow the paths of least resistance through the fractures.

The channel network concept (Gylling et al., 1999; Dessirier et al., 2018), the chequerboard concept (Hartley et al., 2012, 2017), the geostatistical aperture concepts (Frampton et al., 2018; Frampton et al., 2019; Frampton 2025a,b; Makedonska et al., 2016) and scanning real fracture surfaces (Zou et al., 2015, 2017a, 2017b; Thörn and Fransson, 2015) are different approaches to account for the channelling in the fractures, which will yield different flow and transport properties compared to the simple parallel plate approach.

---

[*] Corresponding author.
E-mail address: martin.stigsson@skb.se (M. Stigsson).

https://doi.org/10.1016/j.ees.2025.10.001
Received 10 June 2025; Received in revised form 25 August 2025; Accepted 6 October 2025
Available online 22 October 2025

The surfaces of bounding rock fractures are self-affine (Mandelbrot, 1985; Russ, 1994; Den Outer et al., 1995) and mono-fractal (Renard et al., 2006; Brodsky et al., 2011; Candela et al., 2012) over at least six orders of magnitude (Candela et al., 2009). This finding can be used to determine the fractures' roughness from exposed fracture surfaces or fracture traces, provided the surfaces or traces are representative samples of the fractures (Stigsson and Mas Ivars, 2018; Stiggson, 2015). It can also be the basis to estimate the variable aperture or void space between the surfaces (Stock and Frampton, 2022, 2025a).

Assuming an initial fracture roughness and knowing that most fractures in old crystalline rock masses have been subjected to shear at least once during their existence (Munier and Talbot, 1993; Viola et al., 2009; Saintot et al., 2011; Mattila and Viola, 2014; Scheiber and Viola, 2018) it is possible to generate realistic synthetic fractures by numerically shearing of fractal surfaces. Numerical shearing is usually both time and computer intensive using for example bonded particles (Itasca, 2014a), discrete elements (Itasca, 2013, 2014b), or finite element approaches (Koyama et al., 2006). It is also possible to use semi-analytical methods making use of force equilibrium of slip and breakage forces (Casagrande et al., 2018). Such methods are fast and has been shown to provide relevant results for soft rocks (Casagrande et al., 2018) as well as harder rocks, as long as the normal stress on the contact areas is less than the fractures' Joint Compressive Strength, JCS (Stigsson and Johansson, 2019, in Stigsson, 2019).

Shearing fractures will result in an offset in the direction of the mean fracture plane and a dilation perpendicular to the plane. The amount of dilation and area in contact is dependent on the normal force acting on the fracture and the initial roughness of the bounding surfaces. From the two bounding surfaces an aperture field may be approximated using different approaches (Oron and Berkowitz, 1998). This synthetic shear will hence create a correlation structure in the aperture field that mimics these of real sheared fractures.

Knowing the aperture field of the fracture enables calculation of the transmissivity of each element by use of the local cubic law, LCL, or different modified versions of the LCL (Trinchero et al., 2024; Stock and Frampton, 2025b). The distributed transmissivities mimicking that of natural fractures with high resistant areas surrounded by low resistance channels. The transport properties of such channelized fractures are preferably studied using a Lagrangian framework (Cvetkovic et al., 1999, 2004; Frampton and Cvetkovic, 2011).

The aim of this study is to improve our understanding of how flow and transport behaviour change due to different initial roughness of fractures and normal stress applied on the fractures when sheared. The study makes use of a semi analytical numerically shearing scheme of synthetically generated fractures of 1 m^2. The size is chosen to be a typical scale between the laboratory and field scales. Parameters varied are JRC, between 4 and 10, and applied normal stress during shearing, between 0.2 and 20 MPa to mimic conditions at the rock mass in Forsmark, Sweden.

2. Methods

The workflow in this study is as follows: 1) generate multiple fractures with different roughness, 2) shear the fractures under different normal stresses, 3) offset the resulting surfaces one element and calculate the resulting aperture field, 4) solve the flow through the fracture using global head gradient parallel and perpendicular to the shear direction, and 5) calculate transport parameters. Each method in the workflow is described below.

2.1. Generating synthetic fractures

Fractures can be regarded as self-affine mono-fractal surfaces (Mandelbrot, 1985; Russ, 1994; Den Outer et al., 1995; Renard et al., 2006; Candela et al., 2009, 2012; Brodsky et al., 2011). Self-affine fractals are defined using two parameters, the fractal dimension and a scaling factor (Stigsson and Mas Ivars, 2018). The dimension is a real number between the topological and Euclidian dimension of the object to have a physical meaning. This means that the dimension of a self-affine surface is a real number between 2 and 3 (a fracture is topologically a plane, a two-dimensional object, defined in a Euclidean three-dimensional space). The fractal dimension is often substituted with the Hurst exponent, H, (Hurst, 1957; Russ, 1994; Stigsson and Mas Ivars, 2018). The relationship between H and the fractal dimension, $D_{surface}$, is (Russ, 1994)

$$H = 3 - D_{Surface} \tag{1}$$

As $D_{surface}$ varies between two and three, H varies between one and zero. The Hurst exponent steers the persistence of the asperities i.e. the long-range correlation, which divide fractal surfaces into three groups. If H is larger than 0.5, the fracture surface has a positive long-range correlation while a fracture surface with H less than 0.5, if such exists, has a negative correlation. A special case is when H exactly equals 0.5, then there is no correlation, and the surface is described as a random walk.

The scaling parameter is commonly defined as the standard deviation of height differences, $\sigma_{\delta h}$, located at a specific distance, Δl, denoted $\sigma_{\delta h}(\Delta l)$ (Brown, 1987; Malinverno, 1990; Odling, 1994; Hong-Fa et al., 2002; Renard et al., 2006; Candela et al., 2009; Johansson and Stille, 2014; Stiggson, 2015; Stigsson and Mas Ivars, 2018; Stock and Frampton 2025a)

From digitised fracture surfaces and traces, the two fractal parameters can be evaluated. These parameters can be used to generate synthetic fractures with equal statistics (Stigsson and Mas Ivars, 2018). The two parameters can be related to the 10 geometrical JRC type curves given in (Barton 1973) according to (Stigsson and Mas Ivars, 2018)

$$JRC = -4.3 + 54.6 \cdot \sigma_{\delta h}(1mm) + 4.3 \cdot H \tag{2}$$

A fast and accurate method to generate synthetic fractures with desired properties is through inverse fast Fourier transform (FFT) of a power spectrum (Saupe, 1988; Gallant et al., 1994; Russ, 1994). The intercept of the power spectrum c_I is calculated as (Stigsson and Mas Ivars, 2018)

$$c_I \simeq \frac{\sigma_{\delta h}(1\nu)^2}{\frac{8}{N^2} \cdot \sum_{f=1}^{(N/2)-1} \left(f^{-(H+1/2)} \cdot \sin(\pi \cdot f/N)\right)^2} \tag{3}$$

where $\sigma_{\delta h}(1\,\nu)$ is the standard deviation of height differences of adjacent vertices, f is the frequency, i.e. number of waves per trace length, N is the number of vertices of the fractal line and H the Hurst exponent. The relationship between the slope of the power spectrum, β_{ps}, and H is (Russ, 1994; Stigsson and Mas Ivars, 2018):

$$\beta_{ps} = 2H + 1 \tag{4}$$

Using c_I and β_{ps} the power spectrum of frequencies is generated. This power spectrum together with a random phase shift is used as input to the inverse FFT algorithm to generate a fracture with realistic properties.

2.2. Shearing the fractures

Rock masses usually host numerous discontinuities that may have more or less void. Fractures generated in tensile mode, by the cooling of the rock mass, will have almost mated surfaces resulting in small residual voids, given that only normal forces have been acting. However, if a shear force, large enough, is acting on the discontinuity, a fracture with larger void will be created. A vast majority of old fractures in crystalline rock has been subjected to shear at least once during it existence (Munier and Talbot, 1993; Viola et al., 2009; Saintot et al., 2011; Mattila and Viola, 2014; Scheiber and Viola, 2018). Hence, the creation of synthetic fractures could be done by shearing fractal

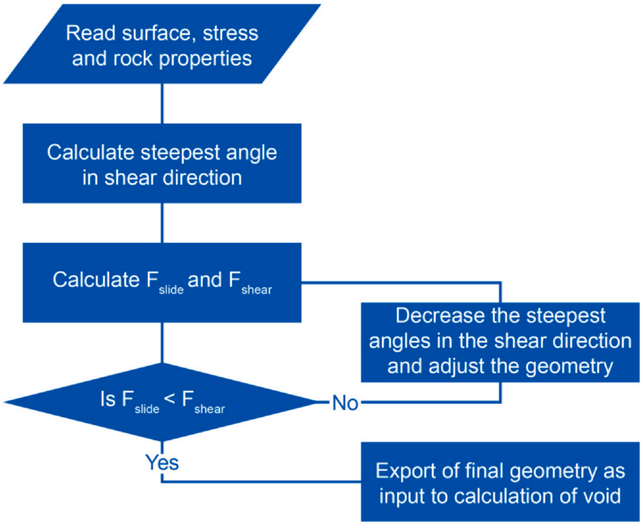

Fig. 1. Flow chart of the simplified shear algorithm (Casagrande et al., 2018).

surfaces. Numerical shearing can be done using different methods such as bonded particles or discrete elements (Itasca, 2013, 2014a, 2014b). However, these methods are computationally demanding. A less demanding method to generate aperture fields is the number swapping algorithm (Ogilvie et al., 2006). The algorithm swaps the random phase shifts in the FFT to match interpreted correlations between different wavelengths on real fractures. Hence, the method needs the correlation structure of real sheared fractures as input to be able to generate synthetically sheared fractures with equivalent properties. Another fast and simple method is to make use of the relationship between the force to break the rock and the force to prohibit slip. This relationship can be used in a semi analytical method to find the peak shear strength of digitised fracture surfaces (Casagrande et al., 2018), which is employed in this study. Assuming that the fracture surfaces will slip when the peak is reached, the method can be used to generate synthetically sheared fractures, starting from perfectly mated rough surfaces. The method makes use of force equilibrium between shearing resistance and sliding resistance. The force to resist shearing, F_{shear}, is calculated according to:

$$F_{shear} = \sum_{cf} (a \cdot c + f_N \cdot \tan(\varphi)) \tag{5}$$

where cf denotes the contributing facets, a is the area of the facet projected on the horizontal plane, c is the cohesion of the rock, f_N is the normal force acting on the facet and φ is the friction angle of the intact rock. The force to resist sliding, F_{slide}, is calculated according to:

$$F_{slide} = \sum_{cf} f_N \cdot \tan(\varphi_b + \beta_{fs}) \tag{6}$$

where φ_b is the basic friction angle of the intact rock and β_{fs} is the slope of the facets contributing to the slide resistance.

The algorithm is visualised in Fig. 1. In brief, the coordinates of the perfectly mated fracture are first read, together with the normal stress acting on the fracture and the properties of the surrounding rock. Thereafter, the geometry is analysed and the facets with the steepest slope in the direction of the shearing are collected to create a set of contributing facets. Using this set of contributing facets, the resistance to slide and resistance to shear asperities are calculated according to Eq. 5 and eq. 6. If sliding resistance is larger than shearing resistance, the forces acting on the fracture surface can be assumed to be large enough to shear off the steepest asperities, resulting in a slightly changed topography of the fracture surface. The new topography is used to find the new set of contributing facets and new resistance forces are calculated. This loop continues until the sliding resistance is less than the shearing resistance, and sliding may occur, mimicking a constant normal load shearing test. At this stage, the output parameters, including the topography of the damaged surface, are saved. The algorithm is suitable for predicting peak and residual shear strength for relatively soft rock fractures (Casagrande et al., 2018). The method has a limit in the sense that the rock mass is assumed rigid. This will result in too high contact stresses for hard rocks. The method gives reasonable results also for hard rocks, such as granites, if conditioned such that the contact stress does not exceed the JCS (Stigsson and Johansson, 2019, in Stigsson, 2019). Due to the implemented method not considering the deformability of the rock mass; mimicking constant normal load conditions; and that it only regard the relationship between the sliding force and shear force, there is no force counteracting any slip movement once the peak is reached. Hence, the surface may slip an infinite amount. It was decided to slide the residual topography of the adjusted upper surface the smallest amount possible, i.e. one element which equals 1 mm, on top of the residual topography of the adjusted lower surface.

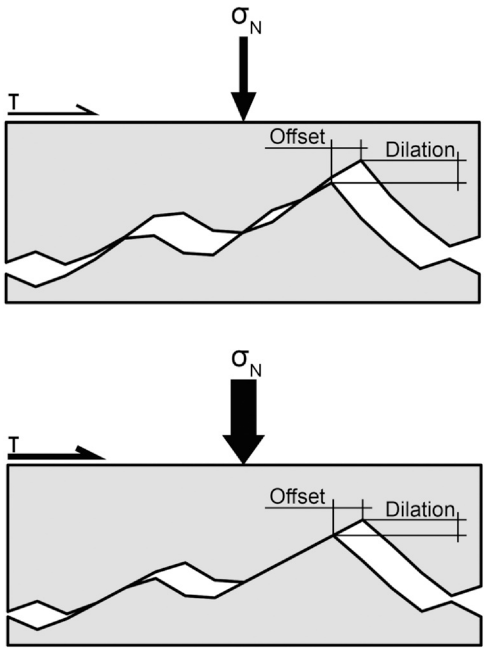

Fig. 2. Resulting aperture distribution due to different normal stresses. Bolder arrows indicate larger values of the forces, resulting in smaller dilation.

2.3. Aperture field

During shearing the damaged fracture surface attains a different geometry compared to the original pristine fracture surface. This adjusted fracture surface is used to create the aperture field of the fracture by letting the upper surface slide an arbitrary distance on the lower surface. Since different normal stress during the force equilibrium iteration will generate different geometry, the aperture field will be different for different normal stresses, see simplified 2D sketch in Fig. 2.

The upper and lower bounding surfaces will not be parallel after the shearing and hence the calculation of a representative aperture for each element is delicate. Many applications simply use the average plane (i.e. the plane that have equal distance in the z direction between the corners of the average surface and the corners of bounding upper and lower surfaces) to calculate the difference in z direction as an approximation of the aperture. This approach will overestimate the aperture where the error will be larger the steeper the elements. The aperture may instead be approximated using the midplane, defined as the plane that has the average direction of the bounding upper and lower surfaces. This results in distances, between the midplane and the bounding planes, that are always equal along the normal vector of the midplane.

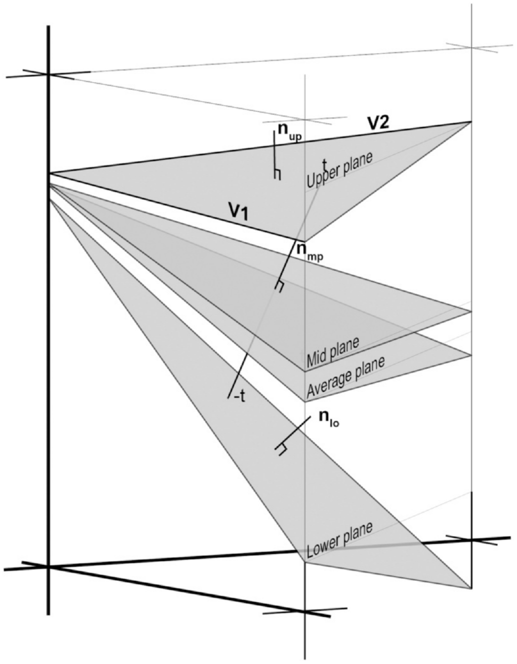

Fig. 3. Definition of aperture, 2 t, of a finite element. The average plane is created by using the mean value of the coordinates defining the computational element. The midplane is the plane where the dihedral angle to the upper and lower plane is equal.

Integrating all these distances over the midplane element surface and calculating the average distance, will equal the distance between the bounding surfaces along the normal vector of the midplane passing through the centroid of the midplane surface element see Fig. 3. This approach is used to assign each computational element its aperture.

2.4. Fracture flow

Under the assumption that 1) fractures are infinite parallel plates 2) water is a Newtonian fluid, 3) there is no-slip between fluid and bounding surfaces, 4) Darcy's law is valid, and 5) steady state conditions prevail, the transmissivity of a fracture can be calculated using the cubic law, CL, (Zimmerman and Bodvarsson, 1994; Gustafson, 2012)

$$T = \frac{\rho g}{\mu} \cdot \frac{a^3}{12} \tag{7}$$

Where T is the transmissivity, ρ the density, g the gravitational acceleration, μ the viscosity and a the aperture.

In reality, fractures are not parallel plates, but instead are the void space between two finite rough surfaces, which violates two of the assumptions for the CL. Even if a rough walled fracture is divided into elements where the Local Cubic Law, LCL, is applied the elements are not parallel as shown in Fig. 2 and Fig. 3. There are many studies (Brush and Thomson, 2003; Yeo and Ge, 2005; Lee and Ahn, 2004; Wang et al., 2015; Zou, 2017a; Trinchero et al., 2024; Stock and Frampton, 2025b) showing that the LCL overestimates the flow through a rough-walled fracture. However, the approach may be reasonable if the local plane is large compared to the aperture; the variance in asperities is small within the element; the opening angle is moderate; and Reynolds number, Re, is small (Oron and Berkowitz, 1998). The effective transmissivity of a fracture stabilises when Re become less than about 4 (Zou, 2017a). At depth, under natural gradients, the flow velocity will be small resulting in small Re; the nature of fractals is such that the small scaled roughness will be less pronounced the smaller the window, resulting in smaller variance of asperities as the element gets smaller; and flow will preferentially flow along paths of large aperture resulting in small changes in opening angle. However, the preference of finding large apertures might violate the criteria of aperture being small compared to the size of the computational elements. This is compensated for as the shearing will create large channels on the leeside of the ridges in the direction of the shear, see Fig. 2, where the extension will be greater than the thickness.

Well aware of the overestimation of flow through a synthetic fracture using LCL assumption compared to solving the full Navier-Stokes equation, the former is used due to its simplicity and the that the absolute numbers are of less interest in this study, compared to the relative flow and transport parameters. The flow is numerically solved using linear triangular finite elements under stationary conditions by the computer code MAFIC (Golder Associates, 2001). MAFIC employs a Galerkin finite element solution scheme to approximately solve the volume conservation equation for two dimensions. The particles will, hence, follow straight paths across each finite element parallel to the gradient.

The transmissivty and aperture of the parallel plate equivalents for each realisation are back calculated to result in the same flux through the parallel plate as through each rough surfaced fracture.

2.5. Transport parameters

Presuming that the conditions for LCL are fulfilled, a single fracture can be divided into several small local elements with different transmissivities assigned according to the local aperture, see Fig. 3. These local elements can be used as finite elements for solving the flow through the fracture, using e.g. a Galerkin finite element scheme. By assigning boundary conditions to the fracture, the hydraulic head can be solved for the corners of all the local elements. Knowing both the hydraulic head of the corners and the geometry of the local element, the head gradient vector, $\mathbf{i}_e$, acting on the element can be calculated. This head gradient vector can be used to calculate the velocity vector, $\mathbf{v}_e$, of the element as:

$$\mathbf{v}_e = a^2 \frac{\rho g}{12\mu} \mathbf{i}_e \tag{8}$$

This specification of the flow field represents the Eulerian flow field, i.e. the flow is a function of position and time, expressed as:

$$\mathbf{v}(\mathbf{x}, t) \tag{9}$$

where $\mathbf{v}$ is the velocity at location $\mathbf{x}$ and time t.

It has been proposed that the Lagrangian specification of the flow field is better suited to handle the advection-dominated transport in fractures (Dagan et al., 1992; Cvetkovic et al., 1999). The Lagrangian specification of the flow field follows the fluid along the flow path in time and space, and is expressed as:

$$\mathbf{X}(\mathbf{x}_0, t) \tag{10}$$

where $\mathbf{X}$ is the location at time t and $\mathbf{x}_0$ is the location at some initial time t_0. The Lagrangian flow field can be obtained by conducting advective particle tracking for indivisible, non-interacting particles with density equal to that of the fluid. Following such particles through one of the local finite elements, which has constant properties, the advective residence time, $\Delta\tau$, in the local element can be expressed as:

$$\Delta\tau = \frac{\mathrm{l}}{\mathrm{v}} \tag{11}$$

where l is the length of the flow path in the element and v is the velocity of the liquid flowing through the element. The total residence time, τ, in the fracture is simply the sum of all residence times along the flow path of the fracture, calculated as:

$$\tau = \sum_{i \in E} \Delta\tau_i = \sum_{i \in E} \frac{\mathrm{l}_i}{\mathrm{v}_i} \tag{12}$$

where i is an element number of the set of local elements, E, visited along the flow path.

Table 1
Parameters used to generate the rough walled fractures.

JRC (-)	H (-)	$\sigma_{\delta h}$(1 mm) (mm)
4	0.7	0.0969
7	0.8	0.1440
10	0.9	0.1910

Table 2
Properties of rock surrounding the synthetic fracture.

Parameter	Value	Unit	Reference
Friction angle, φ	60	°	Table 7–3, (SKB, 2008)
Basic friction angle, φ_b	30	°	Table 4–13, (Glamheden and Curtis, 2006)
Cohesion, c	28	MPa	Table 7–3, (SKB, 2008)

To incorporate reactive exchange processes along the advective paths, an additional segment variable, the transport resistance, β_{tr}, is needed (Cvetkovic et al., 2004). The transport resistance for a local element, $\Delta\beta_{tr}$, which has constant properties, is described by:

$$\Delta\beta_{tr} = \frac{l}{v \cdot b} \tag{13}$$

where b is the half aperture of the element, i.e. $a/2$. As for the total residence time, the total transport resistance, β_{tr}, can be calculated by adding together the local transport resistances along the path:

$$\beta_{tr} = \sum_{i \in E} \Delta\beta_{tr,i} = \sum_{i \in E} \frac{l_i}{v_i \cdot b_i} \tag{14}$$

There is hence a perfect correlation between the residence time and the transport resistance if the half aperture, b_i is constant, as for the parallel plate approach:

$$\beta_{tr} = \frac{1}{b}\tau \tag{15}$$

where $1/b$ is the definition of specific surface area or specific flow wetted surface (Moreno and Neretnieks, 1993; Wels et al., 1996). The specific flow wetted surface is hence the total fracture area with which a volume of liquid is in contact. However, for a rough fracture the aperture is not constant, but varies for each local element along the flow path. For such a path, an effective specific surface area, ω, can be calculated as (Cvetkovic and Frampton, 2012; Cvetkovic and Gotovac, 2013):

$$\omega = \frac{\beta_{tr}}{\tau} \tag{16}$$

The distributions of the four parameters, travel length, l, travel time τ, transport resistance, β_{tr}, and specific flow-wetted surface, ω, are used to show how the flow and transport properties of sheared fractures change due to normal stress and roughness.

Table 3
Stress dependence of friction angle.

Normal stress (MPa)	Φ (°)	JCS* (MPa)
0.2	60	209
2.0	50	153
20.0	30	97

* using Eq. 17

3. Model setup

To investigate how the flow and transport properties changes due to stress and roughness a square, 1 m^2, fracture is used, with element resolution of 1 mm, i.e. each fracture consists of $2{\cdot}10^6$ triangular finite elements of 0.5 mm^2. Generating synthetic fractures using fast Fourier transform, results in surfaces with $2^{\,N}$ unique nodes on each side of the square. However, the first row and column of vertices need to be repeated, resulting in a surface with $2^{\,N} + 1$ by $2^{\,N} + 1$ nodes, to achieve a correct fractal surface. To avoid the most obvious edge effects, such as the repetitive behaviour of Fourier series, the generated surface must be at least four times as large as the surface to extract. Thus, fractures of 2048 × 2048 elements (2049 × 2049 vertices) are generated to be able to extract a 1 m^2 square fracture with resolution 1 mm. The fractures are generated with three different roughness, corresponding to JRC 4, 7 and 10, calculated according to Eq. 2 (Stigsson and Mas Ivars, 2018), see Table 1. Using Monte Carlo realisations, 128 fractures are generated for each roughness to get stable median values of the investigated metrics. To get stable metrics for the variance many more realisations would be needed due to the surfaces' being fractal and, hence, resulting in more volatile results in the tail of the result distributions. This means that results above 99th percentile, in Figs. 7–14 and Tables 4–7, should be used with caution.

The properties of the rock mass are taken from the site investigations performed by SKB at Forsmark (SKB, 2008), see Table 2.

Using the parameters in Table 2, the joint compressive strength, JCS, is 209 MPa when calculated as (Barton 1973) for a fracture without alteration or infilling:

$$JCS = \frac{2 \cdot c \cdot \cos(\varphi)}{1 - \sin(\varphi)} \tag{17}$$

where c denotes cohesion of the intact rock and φ is the friction angle of the intact rock.

From the generated surfaces, with 2049 × 2049 vertices, squares of 1025 × 1025 vertices are extracted to construct surfaces with 1024 × 1024 elements. These surfaces are run through the employed shear algorithm, Fig. 1, to create the adjusted topography under three different levels of normal stress, 0.2, 2.0 and 20.0 MPa.

Now, when the rock is competent, as a granite, sliding will occur on steep facets, despite high normal loads, due to the assumption in the shearing algorithm that the rock is rigid. The normal stresses on the contributing facets can hence be larger than JCS, which is not possible for a real rock. To compensate for the damage and count for the elastic and plastic deformation, the internal friction angle of the rock is lowered at the contributing elements until $\sigma_N <$ JCS. This results in a stress dependent friction angle according to Table 3. As seen, JCS decrease as the friction angle decrease, but the area of contributing facets increases faster as JCS decreases, and hence, σ_N becomes less than JCS

After the shear force algorithm has been applied, the upper rock surface is slided one vertex, i.e. 1 mm, along the steepest residual slopes in the direction of the shear force, see Fig. 2. This results in a fracture, with voids, defined by 1024 × 1025 vertices. From these two bounding geometries, a square fracture of 1001 × 1001 vertices (I.e. 1000 × 1000 times 2 finite elements) is extracted, from which, the average surface for each computaional finite element is calculated to get a continuous fracture, Fig. 3. All elements are then assigned an aperture using the perpendicular aperture at the centroid of the mid-plane element, Fig. 3, and transmissivity is calculated according to cubic law, Eq. 7. The flow field and transport of particles are solved for a global unit gradient in two directions: 1) global gradient is parallel to the shear direction and 2) global gradient is perpendicular to the shear direction. The upstream boundary is given a 1 m larger head than the downstream boundary and the other two sides of the surface are not given any boundary condition, which equals a no flow boundary. As the basis for the Lagrangian framework, 10,000 particles are released, flux weighted, on the upper flow boundary, i.e. the larger the flux, the

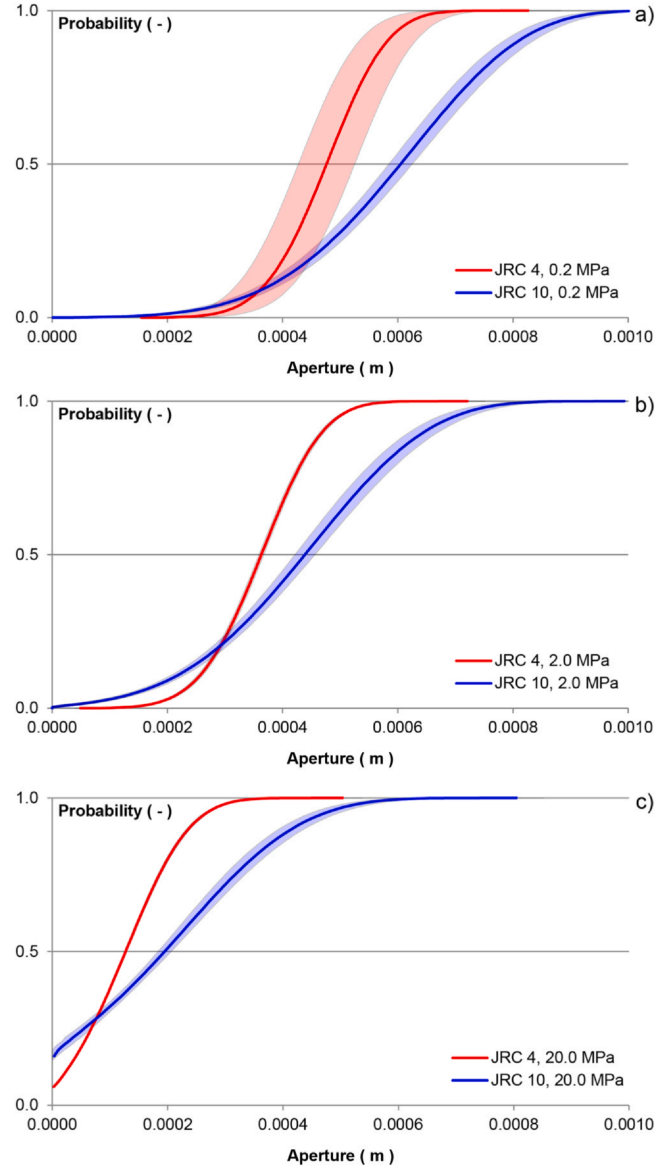

Fig. 4. The change in aperture distribution depending on stress and roughness. (top) 0.2 MPa, (middle) 2.0 MPa and (bottom) 20 MPa normal stress. (red) smooth, (purple) intermediate and (blue) rough initial bounding surfaces, together with shaded 95 percentile confidence of generated apertures.

higher the probability that a particle will be released anywhere along the border of that element.

4. Results

To make the differences between the realisation ensembles more visible, CDF's (Cumulative Distribution Function), are used for high resolution of low values and CCDF's (Complementary Cumulative Distribution Function) are used for high resolution of large values.

The numerical shearing of the realistic synthetic fractures give rise to different aperture distributions depending on the roughness of the bounding surfaces and the applied normal force when sheared, see Fig. 4. When the normal stress is increased the apertures decrease. The median aperture gets smaller, but the variance of the aperture field keeps about constant. Under low stress the aperture distribution conforms to a normal distribution, but as the normal stress increases, and thereby the area of contact, the distribution becomes more truncated. The roughness of the fracture will alter both the variance and the median of the aperture distribution; an increase in roughness will increase both values. There is also a slight change in the distribution type where the rougher surfaces generate longer tails for the aperture distribution than a normal distribution will yield.

It is not only the aperture distribution itself that is important for flow and transport, but even more so, the correlation structures of the aperture that arise. Shearing the bounding surfaces will result in correlation structures that is anisotropic, usually larger perpendicular to the direction of the shear. These areas, or channels, arise behind the ridges in the direction of shear, i.e. on the leeside. On the push side, the bounding surfaces of the fracture will be in contact, or have small apertures, see Fig. 5.

The pattern of the particle traces will differ depending on the correlation structure where fractures with rougher bounding surfaces and higher normal stress will have more tortuous paths than smoother fractures and fractures subjected to less stress. When the fracture is smooth, JRC = 4, and under a low pressure, 0.2 MPa, the traces will be almost straight lines from upstream to downstream boundary, see upper left in Fig. 6. When the fracture is rough, JRC = 10, and under large stress, 20 MPa, there will be many paths that are perpendicular or even opposite to the global gradient of the fracture, see lower right in Fig. 6. These different behaviours are investigated using a Lagrangian framework with 10,000 particles released, flux weighted, at the upper flow boundary. Despite a finite element solver and sometimes complex geometry of the fracture surface the average recovery of particles for each parameter combination varies between 100 % and 96.5 %. The lower recovery relates to rougher fractures subjected to higher normal stress, due to the more complex geometry that may result in dead end voids where particles can get stuck as a result of small errors in the mass balance due to the usage of a finite element scheme solving the flow.

4.1. Travel paths

The travel length for any particle released on the upstream boundary of a square homogeneous fracture, i.e. a parallel plate, will result in a travel distance equal to the length of the fracture, in this case 1 m. As soon as the geometry and aperture field vary spatially, the flow paths will find the route of least flow resistance from the starting position on the upstream boundary to the outlet at the downstream boundary (Fig. 6). This will result in a distribution of path lengths. Depending on the spatial distribution of areas in contact and areas of low conductance, the paths will be more or less tortuous. This is clearly apparent in Fig. 6 to Fig. 8. For global gradient parallel to the shear direction, Fig. 7 and Table 4, the traces are longer the rougher the fracture (a *vs* b, c *vs* d, e *vs* f) and the larger the normal force applied (a *vs* e, b *vs* f). Further, the variance and the difference between shortest and longest paths, increases between different realisations as the roughness and normal stress increase. The same pattern is also apparent in the case of gradient perpendicular to the shear direction, but less pronounced, Fig. 8 and Table 4. There is one major difference, however. The shortest paths for flow perpendicular to the shear direction were all less than 1.1 m, irrespective of roughness or stress, while there was a clear difference in the shortest paths in the case of gradient parallel to the shear direction, due to roughness and normal stress. The median travel length, i.e. 50th percentile, for gradient parallel to shear direction, was about 10 % larger as roughness increases and about 50 % as normal stress increases. The corresponding numbers for gradient perpendicular to shear is 3 % and 10 % respectively.

The explanation of the short paths when global gradient is perpendicular to the shear direction is that the shearing creates continuous large aperture channels behind the ridges of the fracture surface where the particles can easily travel, Fig. 6. When the global gradient is aligned with the shear, the particles will use the same channels to find their way around obstacles such as areas of low aperture or contact. This means that the particles take long paths perpendicular to the global gradient to find channels that bypass the obstacles, and hence the travel length becomes much longer, Fig. 6.

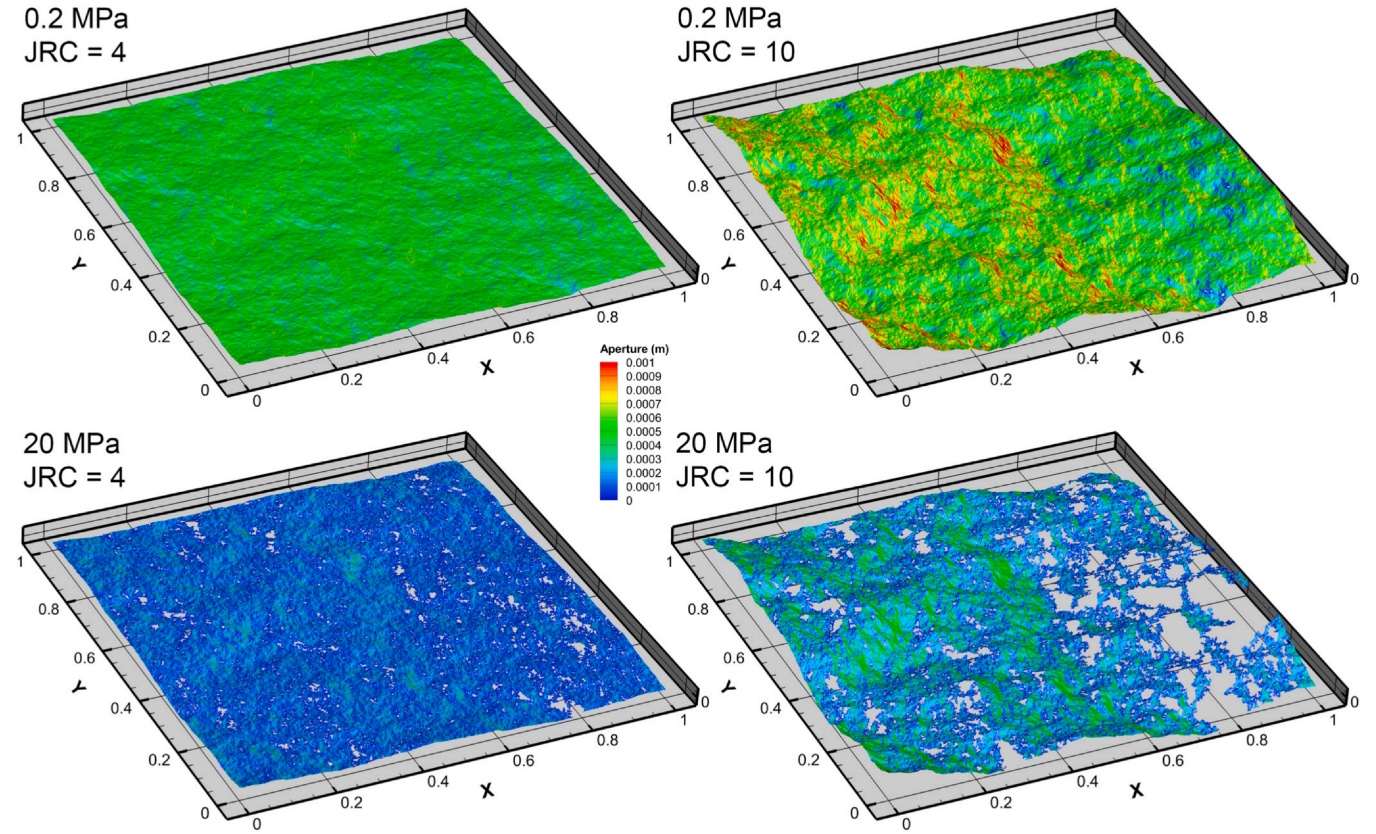

Fig. 5. Example of aperture distribution of, in x-direction, sheared fractures using different initial roughness and normal stress. (Upper row) 0.2 MPa, (Lower row) 20 MPa, (Left column) JRC 4 and (right column) JRC 10. Observe that the z-axis is scaled 2.25 times the x and y axes.

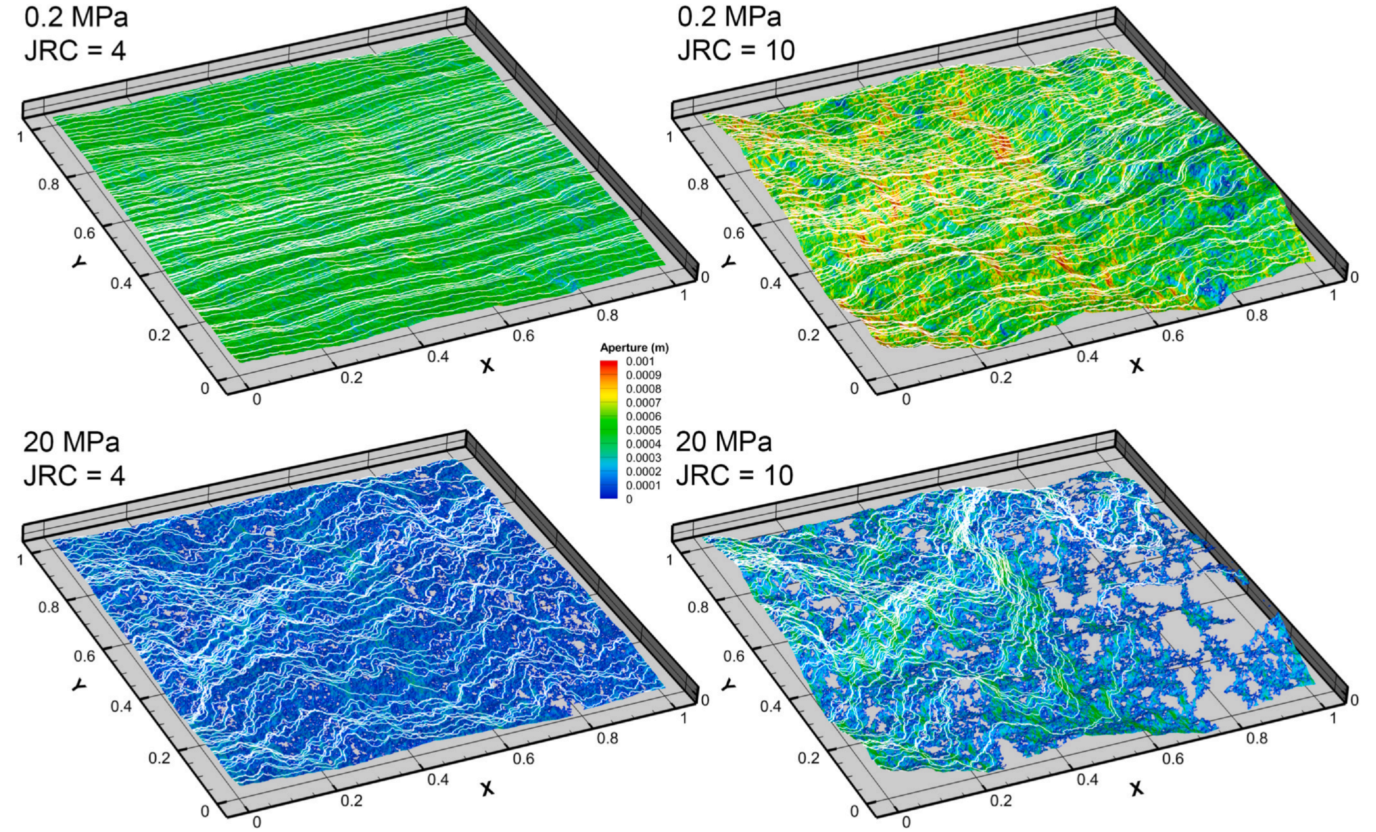

Fig. 6. Example of traces (white) from 100 of the 10000 particles flowing through the fractures of different initial roughness and normal stress. (Upper row) 0.2 MPa, (Lower row) 20 MPa, (Left column) JRC 4 and (right column) JRC 10. Observe that the z-axis is scaled 2.25 times the x and y axes.

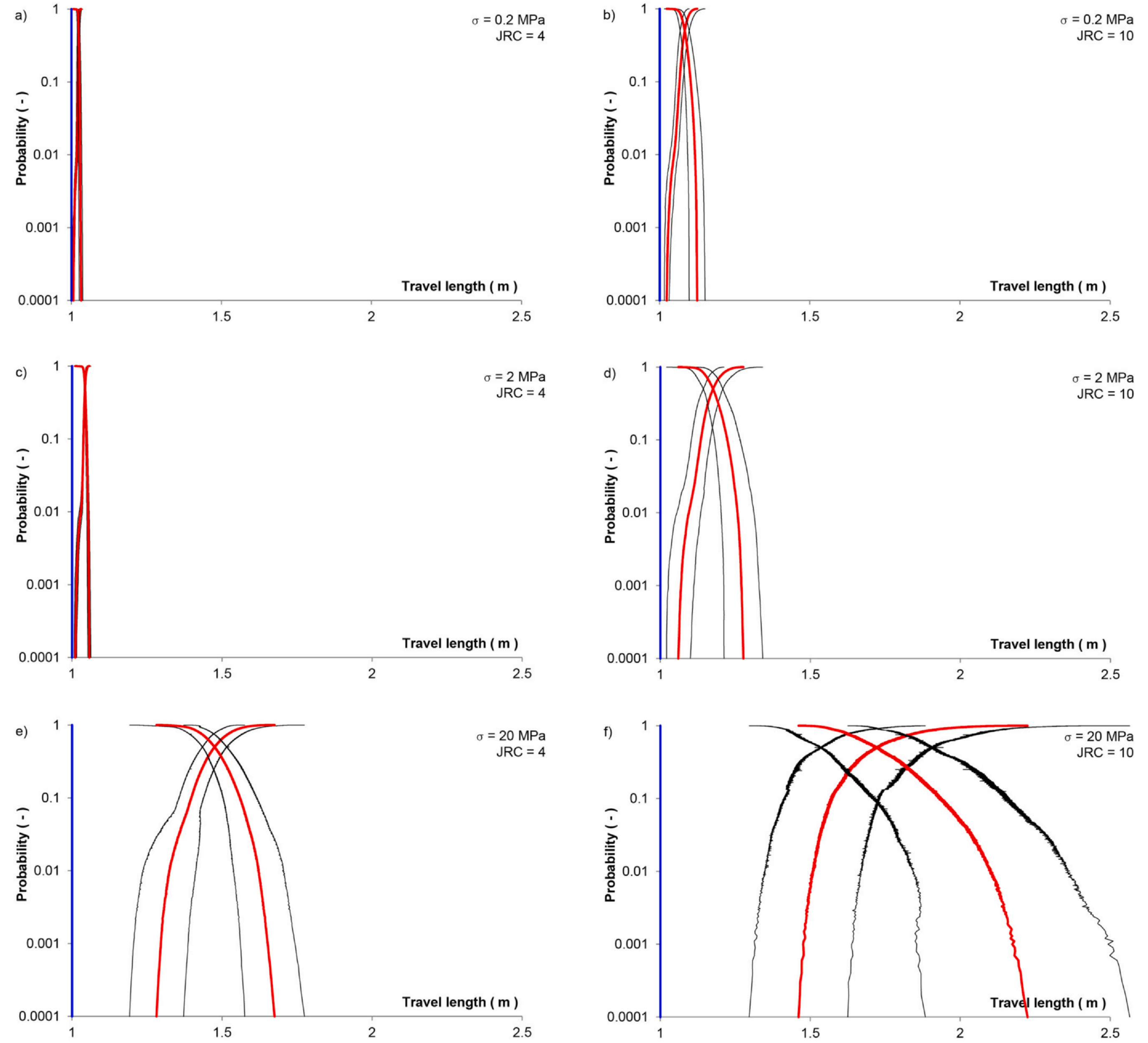

Fig. 7. CDF and CCDF of travel length. Global gradient parallel to shear direction. Red line is average of 128 realisations, black lines are inferred 2σ spread, and blue lines are values for equivalent parallel plate. (Upper row) 0.2 MPa, (middle row) 2 MPa, (lower row) 20 MPa, (Left column) JRC = 4, (right column) JRC = 10.

Table 4
Selected percentiles of lengths of travel path from the CDF's in Figs. 7 and 8 together with the values from the parallel plate equivalent.

σ	JRC	∇	1 %	10 %	50 %	90 %	*99 %*[*]	parallel
0.2	4	X	1.018	1.022	1.024	1.027	*1.029*	1.000
0.2	10	X	1.048	1.066	1.083	1.103	*1.118*	1.000
2	4	X	1.029	1.038	1.043	1.049	*1.053*	1.000
2	10	X	1.095	1.135	1.176	1.222	*1.257*	1.000
20	4	X	1.324	1.397	1.475	1.559	*1.620*	1.000
20	10	X	1.507	1.571	1.723	1.930	*2.103*	1.000
0.2	4	Y	1.015	1.017	1.020	1.023	*1.025*	1.000
0.2	10	Y	1.033	1.038	1.047	1.060	*1.071*	1.000
2	4	Y	1.022	1.026	1.030	1.035	*1.039*	1.000
2	10	Y	1.044	1.052	1.066	1.089	*1.109*	1.000
20	4	Y	1.087	1.100	1.123	1.157	*1.195*	1.000
20	10	Y	1.088	1.103	1.139	1.214	*1.345*	1.000

[*] Observe that the values from the 99th percentile might be biased due to small numerical errors

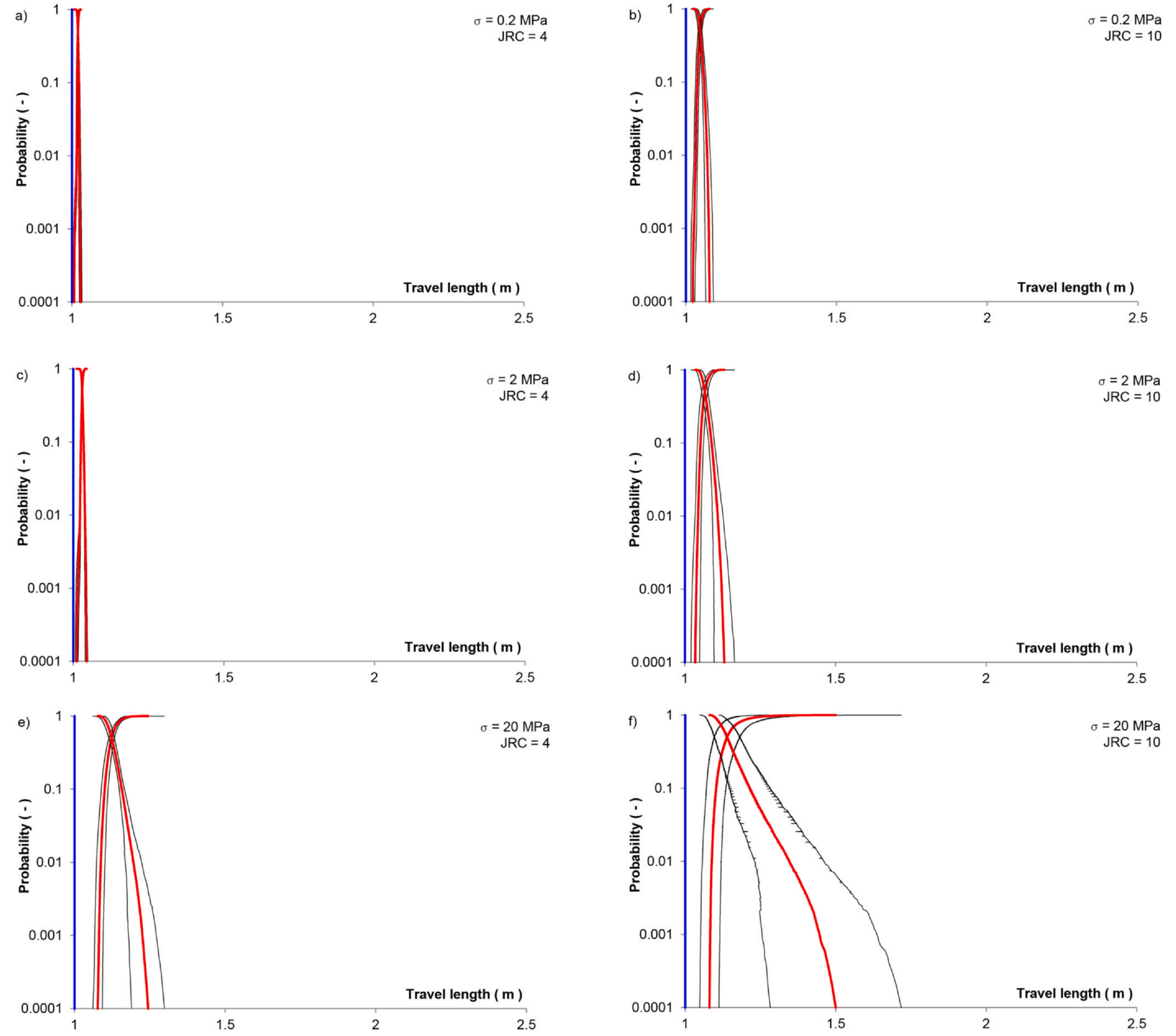

Fig. 8. CDF and CCDF of travel length. Global gradient perpendicular to shear direction. Red line is average of 128 realisations, black lines are inferred 2σ spread, and blue lines are values for equivalent parallel plate. (Upper row) 0.2 MPa, (middle row) 2 MPa, (lower row) 20 MPa, (Left column) JRC = 4, (right column) JRC = 10.

4.2. Travel times

The flow field was numerically solved using a global gradient equal to unity for easy scaling of the results. Such gradient is not anticipated to exist at great depth in rock masses under natural conditions and it results in unrealistic high flow velocities and short residence times in the fracture. The gradient is not relevant when solving the flow using Reynolds lubrication equation, since the velocity and travel times scale linearly to the gradient, Eq. 8. Using a Navier-Stokes solver, however, such a gradient would severely affect the results due to the formation of eddies, resulting in longer residence times.

The distributions of travel times are shown in Fig. 9 for global gradient parallel to shear direction and Fig. 10 for global gradient perpendicular to shear direction. The travel time for a few selected percentiles together with the equivalent parallel plate are presented in Table 5. The travel times for flow along the shear direction were about one and a half order of magnitude larger for the fastest particles (1st percentile); more than three orders of magnitude larger for the slow particles (99th percentile); and about 50 times larger for the median value when the normal stress was increased 100 times, no matter the roughness, Fig. 9, a *vs* e, b *vs* f, and Table 5. Increasing roughness, the travel time decrease for the fast and median speed particles, but show a non-consistent behaviour for the slow particles, Fig. 9(a *vs* b, c *vs* d, e vs f). The overall pattern is though that the travel time decreases with increased roughness.

For the cases with global gradient perpendicular to the shear direction, the travel times for flow along the shear direction were about five to ten times larger for the fastest particles; two and a half to three orders of magnitude larger for the slow particles; and ten to fifteen times larger for the intermediate particles when the normal stress was increased 100 times, Fig. 10 (a *vs* e, b *vs* f) and Table 5. The effect of increasing roughness is not very distinct, but there is a decrease of about a factor two in travel time for the fast and moderate particles. For the slow particles there is a decrease for the low and high stresses (0.2

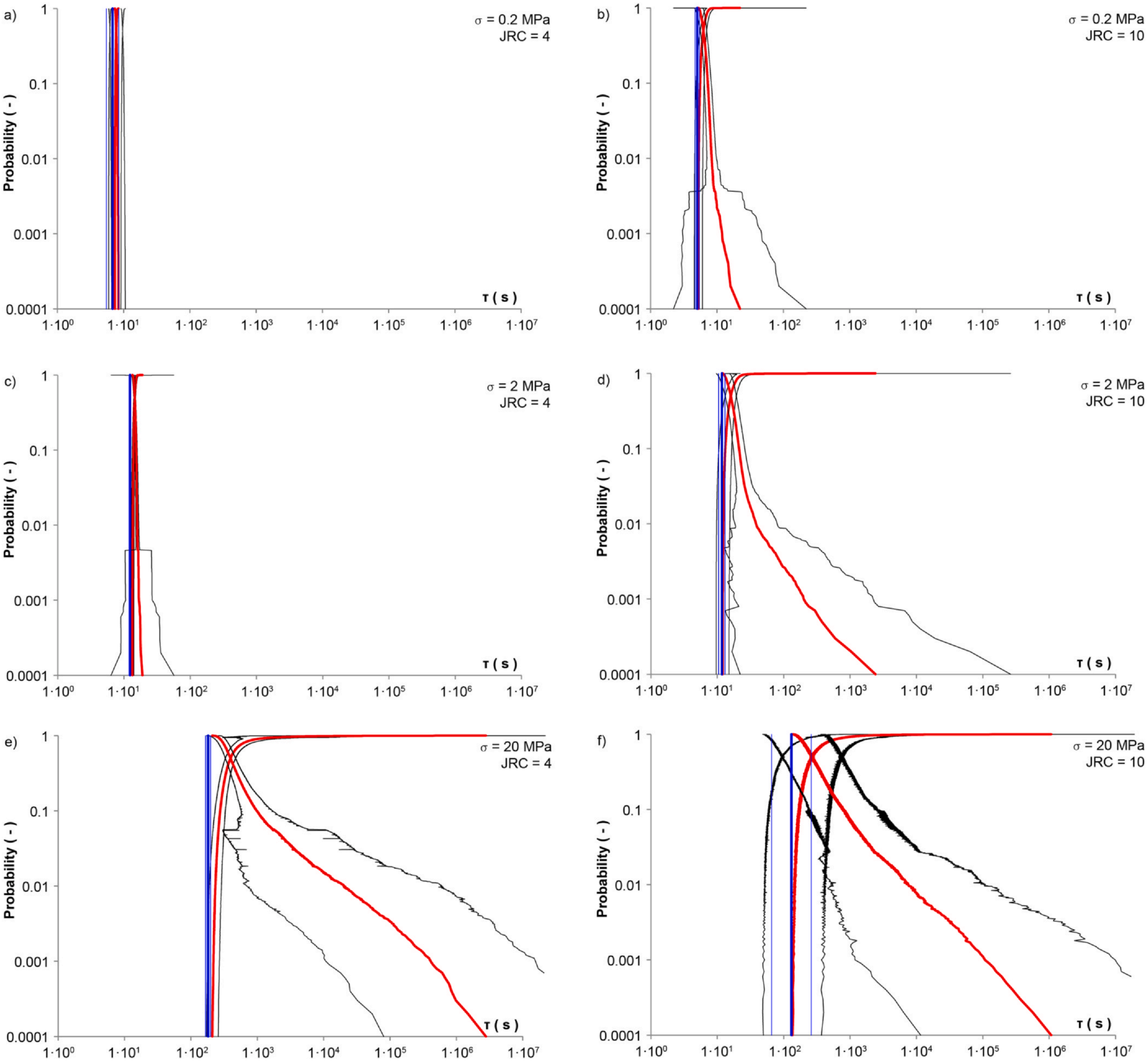

Fig. 9. CDF and CCDF of travel time. Global gradient parallel to shear direction. Red line is average of 128 realisations, black lines are inferred 2σ spread, and blue lines are values for equivalent parallel plate. (Upper row) 0.2 MPa, (middle row) 2 MPa, (lower row) 20 MPa, (Left column) JRC = 4, (right column) JRC = 10.

and 20 MPa) but a small increase for the intermediate stress Fig. 10 (a *vs* b, c *vs* d, e vs f) and Table 5. Despite the flow paths of the rougher fractures being longer than the flow paths of the corresponding smoother fractures, Fig. 8, the fastest travel times are shorter. This can be explained by the rougher surfaces on average having larger apertures with longer correlation length, i.e. the fast channels are more persistent and more conductive. The longer tail can be explained by the longer paths together with more areas in contact or with small apertures, it might also be an artefact of small numerical errors. The variance in travel time, due to different realisations, for fast particles is larger for rough fractures when global gradient is in the shear direction, but less so for global gradient perpendicular to shear. This indicates that continuous highly conductive channels do not occur in every realisation when global gradient is aligned with the shear direction.

For slow particles, there was not much difference regarding the extremely large variance in the tail above about 99th percentile. This indicates that, irrespective of the input parameters, there might be very long particle traces or not present. It may also be an artefact of the limited number of realisations, 128, in combination with fractal surfaces, or the discontinuity in the flow field that may locally occur using a finite element scheme

The travel times for the equivalent parallel plate calculations were in the same range as for the fastest particles through the fractures with rough bounding surfaces when the global gradient was in the direction of the shear, blue lines in Fig. 9, and Table 5. This is explained by the long paths that the particles have to travel through in the fractures with rough bounding surfaces and, even if they find sub-paths with high conductivity, the particles still have to pass through areas of low conductance, slowing them down. When the global gradient is perpendicular to the shear direction, Fig. 10 and Table 5, continuous paths behind the ridges are well connected and hence there are many large aperture paths that are well connected between the upper and lower head boundaries. This implies that the smallest travel times for global gradient perpendicular to shear direction will be much smaller for fractures with rough bounding surfaces than the travel time for an equivalent parallel plate, blue lines in Fig. 10. For the roughest

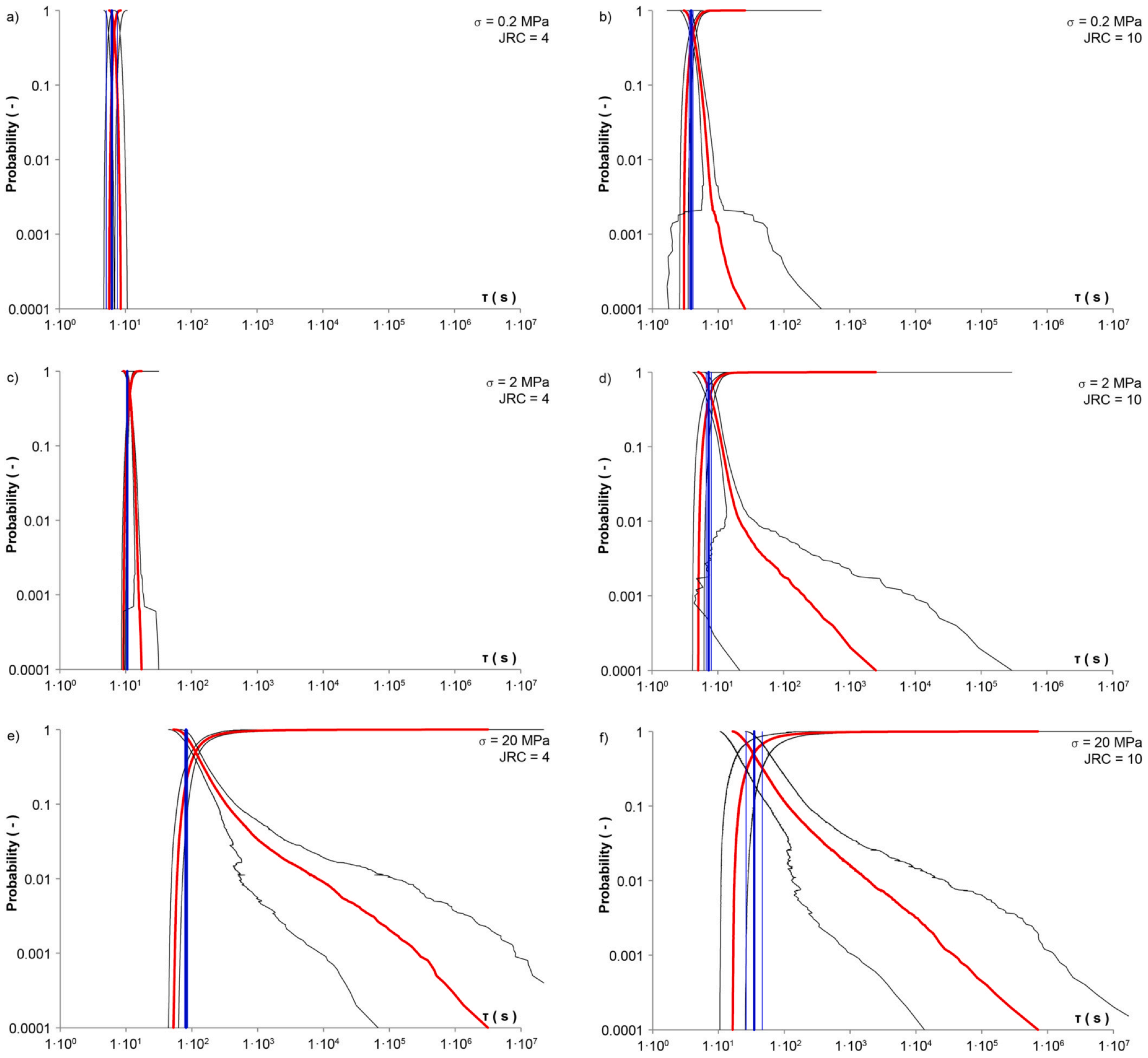

Fig. 10. CDF and CCDF of travel time. Global gradient perpendicular to shear direction. Red line is average of 128 realisations, black lines are inferred 2σ spread, and blue lines are values for equivalent parallel plate. (Upper row) 0.2 MPa, (middle row) 2 MPa, (lower row) 20 MPa, (Left column) JRC = 4, (right column) JRC = 10.

Table 5
Selected percentiles travel time from the CDFs in Figs. 9 and 10 together with the values from the parallel plate equivalent.

σ	JRC	∇	1 %	10 %	50 %	90 %	*99 %*[*]	parallel
0.2	4	X	7.41	7.52	7.75	8.01	*8.17*	6.81
0.2	10	X	5.33	5.57	6.25	7.29	*8.32*	5.03
2	4	X	13.59	13.91	14.55	15.31	*15.90*	12.36
2	10	X	12.29	13.19	15.98	21.25	*38.18*	11.70
20	4	X	233.93	276.40	395.48	982.59	*20338.50*	182.22
20	10	X	143.99	172.68	272.59	781.66	*7487.77*	130.77
0.2	4	Y	5.88	6.22	6.79	7.46	*8.02*	6.23
0.2	10	Y	3.12	3.41	4.18	5.51	*6.97*	3.89
2	4	Y	9.64	10.35	11.59	13.16	*14.56*	10.60
2	10	Y	5.26	5.89	7.70	11.64	*21.57*	7.30
20	4	Y	59.63	72.66	113.94	330.22	*7892.50*	81.94
20	10	Y	17.47	20.53	33.96	112.33	*1859.20*	34.92

[*] Observe that the values from the 99th percentile might be biased due to small numerical errors

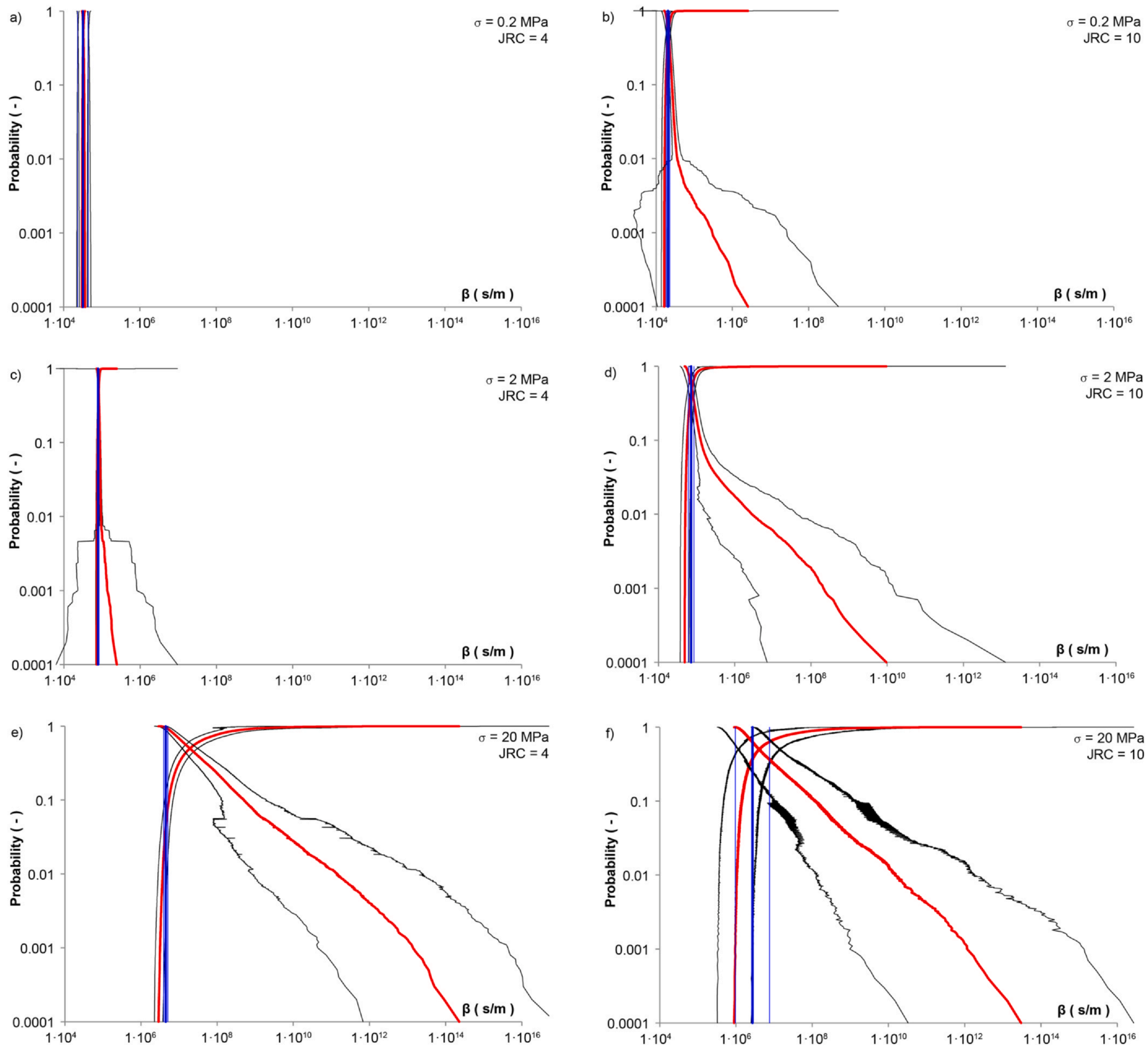

Fig. 11. CDF and CCDF of transport resistance. Global gradient parallel to shear direction. Red line is average of 128 realisations, black lines are inferred 2σ spread, and blue lines are values for equivalent parallel plate. (Upper row) 0.2 MPa, (middle row) 2 MPa, (lower row) 20 MPa, (Left column) JRC = 4, (right column) JRC = 10.

fractures subjected to highest normal stress about 50 % of the particles have lower residence time compared to an equivalent parallel plate approach, making the parallel plate approach non-conservative from safety case view for geological repositories for hazardous waste.

To conclude; using parallel plate approach will result in equal residence times for the fastest particles, when hydraulic gradient is parallel with shear direction, but as the gradient becomes perpendicular, the parallel plate approach will severely overestimate the residence time for the fastest particles.

4.3. Transport resistance

The transport resistance is, as the travel time, dependent on the gradient applied and hence the absolute values are of minor importance, unless scaled using realistic hydraulic gradient. The CDF's and CCDF's for the transport resistance are shown in Fig. 11 (global gradient parallel to the shear direction) and Fig. 12 (global gradient perpendicular to the shear direction) and a few selected percentiles tabulated in Table 6 for the different roughness values and normal stresses.

When the normal stress increases from 0.2 MPa to 20 MPa, the median transport resistance increases 200 times for JRC = 10 Fig. 11 (b *vs* f) and up to 600 times for JRC = 4 (a vs e) for the case where the gradient is parallel with the shear direction. The difference for the fast particles is about a third, i.e. 60–120 times. Due to the very long tails the slow particles may have more than 6 orders of magnitude larger transport resistance when the normal stress is increased 2 orders of magnitude.

Changing the roughness, the median transport resistance decreases with increased roughness, Fig. 11 (a *vs* b, c *vs* d, e *vs* f). The change is small from about 1.5 times to about 5 times for low normal stress (a and b) respectively high normal stress (e and f). For the fast particles the corresponding change is between 2 and 4 times. For the slow particles, transport resistance increases when JRC increases. The increase is about 30 times and hence resulting in larger spread. However, when the

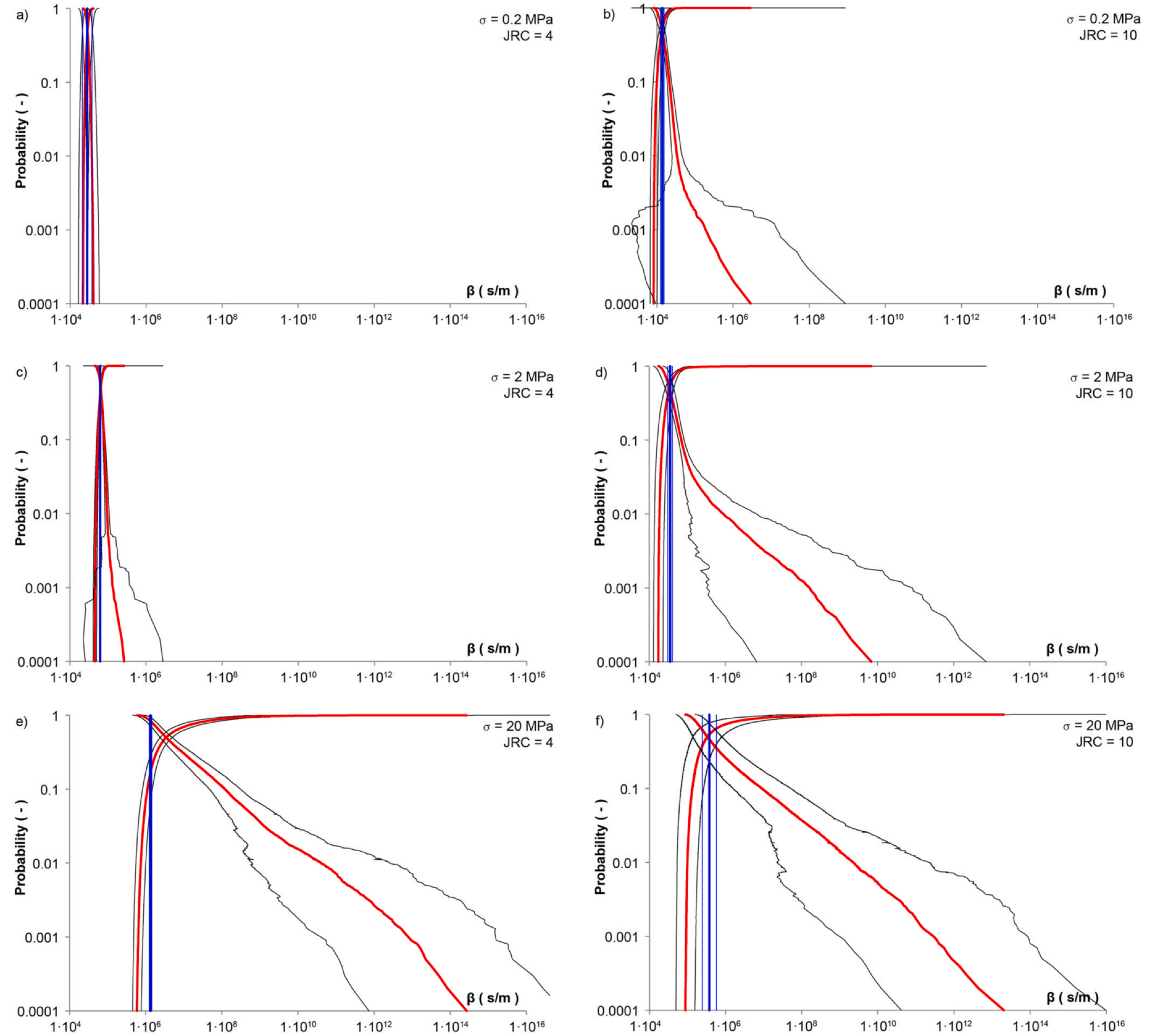

Fig. 12. CDF and CCDF of transport resistance. Global gradient parallel to shear direction. Red line is average of 128 realisations, black lines are inferred 2σ spread, and blue lines are values for equivalent parallel plate. (Upper row) 0.2 MPa, (middle row) 2 MPa, (lower row) 20 MPa, (Left column) JRC = 4, (right column) JRC = 10.

Table 6
Selected percentiles of transport resistance from the CDF's in Figs. 11 and 12 together with the values from the parallel plate equivalent.

σ	JRC	∇	1 %	10 %	50 %	90 %	*99 %*[*]	parallel
0.2	4	X	$3.08\cdot10^{4}$	$3.15\cdot10^{4}$	$3.29\cdot10^{4}$	$3.44\cdot10^{4}$	$3.54\cdot10^{4}$	$3.21\cdot10^{4}$
0.2	10	X	$1.68\cdot10^{4}$	$1.79\cdot10^{4}$	$2.10\cdot10^{4}$	$2.62\cdot10^{4}$	$3.58\cdot10^{4}$	$2.04\cdot10^{4}$
2	4	X	$7.38\cdot10^{4}$	$7.64\cdot10^{4}$	$8.14\cdot10^{4}$	$8.76\cdot10^{4}$	$9.41\cdot10^{4}$	$7.86\cdot10^{4}$
2	10	X	$5.09\cdot10^{4}$	$5.66\cdot10^{4}$	$7.48\cdot10^{4}$	$1.29\cdot10^{5}$	$2.79\cdot10^{6}$	$7.23\cdot10^{4}$
20	4	X	$3.69\cdot10^{6}$	$5.39\cdot10^{6}$	$1.93\cdot10^{7}$	$5.00\cdot10^{8}$	$1.43\cdot10^{11}$	$4.45\cdot10^{6}$
20	10	X	$1.04\cdot10^{6}$	$1.43\cdot10^{6}$	$4.12\cdot10^{6}$	$1.17\cdot10^{8}$	$1.51\cdot10^{10}$	$2.70\cdot10^{6}$
0.2	4	Y	$2.31\cdot10^{4}$	$2.52\cdot10^{4}$	$2.88\cdot10^{4}$	$3.33\cdot10^{4}$	$3.73\cdot10^{4}$	$2.81\cdot10^{4}$
0.2	10	Y	$8.69\cdot10^{3}$	$1.00\cdot10^{4}$	$1.37\cdot10^{4}$	$2.12\cdot10^{4}$	$3.38\cdot10^{4}$	$1.39\cdot10^{4}$
2	4	Y	$4.86\cdot10^{4}$	$5.42\cdot10^{4}$	$6.48\cdot10^{4}$	$7.93\cdot10^{4}$	$9.52\cdot10^{4}$	$6.24\cdot10^{4}$
2	10	Y	$1.87\cdot10^{4}$	$2.25\cdot10^{4}$	$3.44\cdot10^{4}$	$7.03\cdot10^{4}$	$8.81\cdot10^{5}$	$3.56\cdot10^{4}$
20	4	Y	$7.47\cdot10^{5}$	$1.11\cdot10^{6}$	$3.46\cdot10^{6}$	$1.19\cdot10^{8}$	$3.90\cdot10^{10}$	$1.34\cdot10^{6}$
20	10	Y	$9.92\cdot10^{4}$	$1.34\cdot10^{5}$	$3.34\cdot10^{5}$	$8.84\cdot10^{6}$	$2.16\cdot10^{9}$	$3.73\cdot10^{5}$

[*] Observe that the values from the 99th percentile might be biased due to small numerical errors

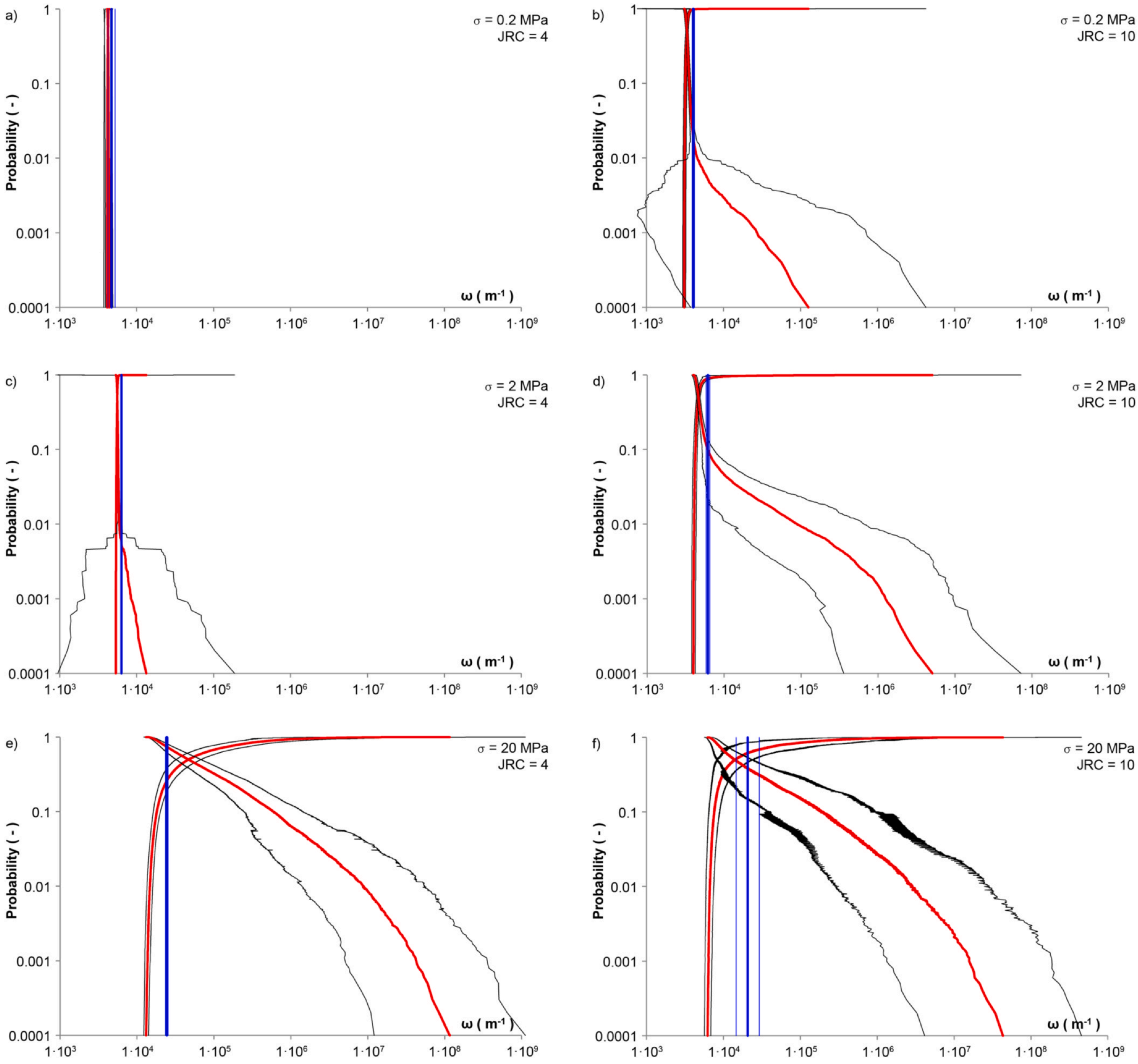

Fig. 13. CDF and CCDF of specific flow wetted surface. Global gradient parallel to shear direction. Red line is average of 128 realisations, black lines are inferred 2σ spread, and blue lines are values for equivalent parallel plate. (Upper row) 0.2 MPa, (middle row) 2 MPa, (lower row) 20 MPa, (Left column) JRC = 4, (right column) JRC = 10.

normal stress is 20 MPa the transport resistance decreases about 10 times as roughness increase from JRC 4 to JRC 10 resulting in about the same spread between fast and slow particles.

The transport resistance, when the global head gradient is perpendicular to the shear direction, follow the same pattern as the case when the head gradient is parallel to the shear direction, but less pronounced, Fig. 12 and Table 6. The fractures with higher JRC generally have lower transport resistance but larger variation in the lower end than the smoother fractures. This is explained by the rougher fractures having a greater probability of developing paths with more persistent large apertures. In the high end, the difference is ambiguous, and the results might be an effect of the pseudo random number generator producing releasing points of particles in low flux areas or small numerical error in the flow solution affecting the particles to enter high transport resistance paths.

The transport resistance, for the equivalent parallel plates, is always higher than the lowest values for the fractures with rough bounding surfaces, and more so as normal stress and JRC increase. This indicates that the parallel plate will, by some amount, overestimate the minimum possible transport resistance, particularly for the case with global gradient perpendicular to shear direction due to the more connected large aperture paths in that direction.

4.4. Specific flow wetted surface

The specific flow wetted surface is the available fracture surface area per volume of water, i.e. the inverse of the half-aperture in a parallel plate approach. For a rough fracture in a Lagrangian framework it is dependent on the half-apertures along flow paths. The mean and inferred 2σ spread in specific flow wetted surface of the 128 Monte Carlo generated fractures are shown in Fig. 13 for global head gradient aligned with the shear direction, and Fig. 14 for global head gradient perpendicular to the shear direction, and a few selected percentiles presented in Table 7.

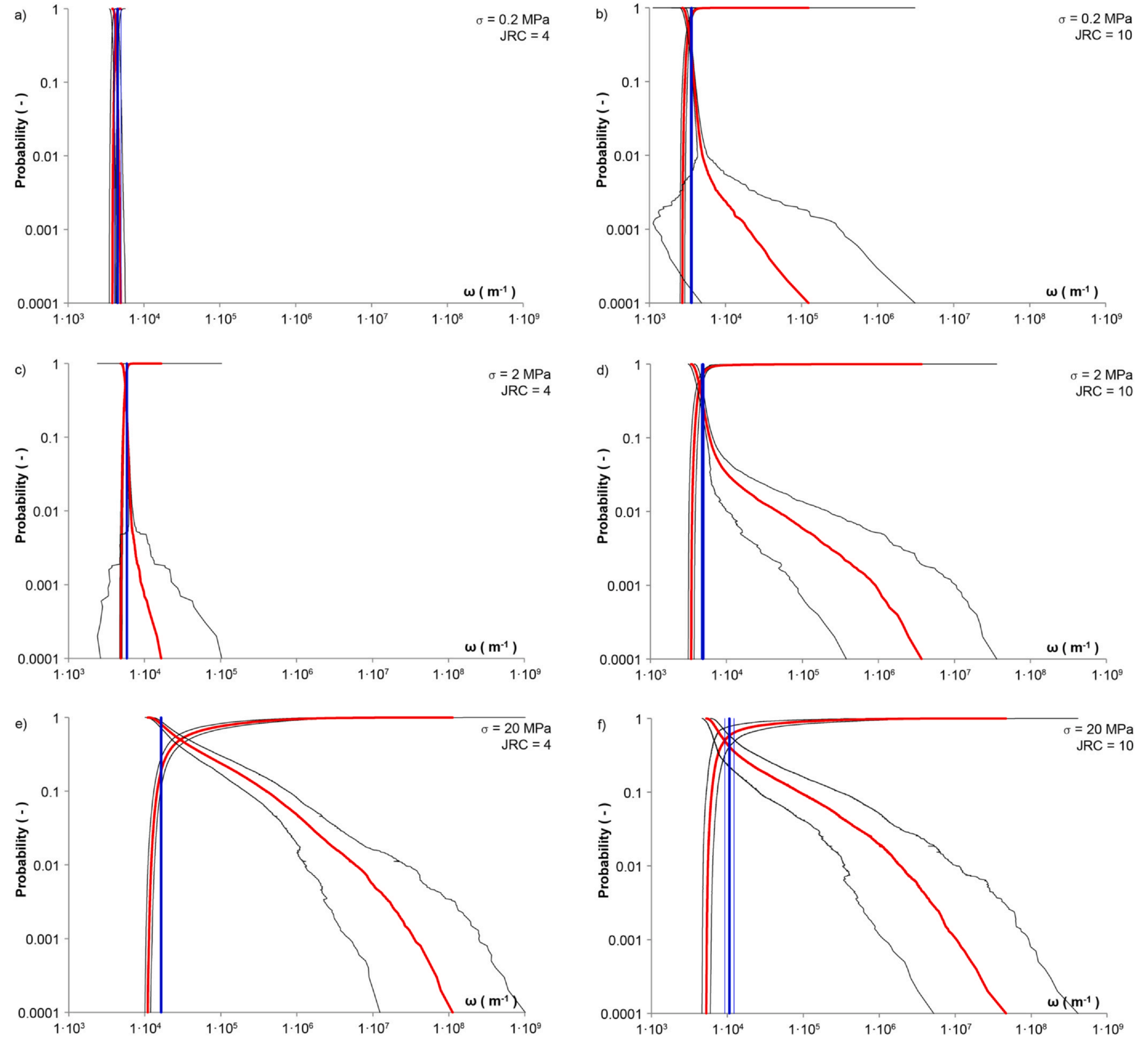

Fig. 14. CDF and CCDF of specific flow wetted surface. Global gradient parallel to shear direction. Red line is average of 128 realisations, black lines are inferred 2σ spread, and blue lines are values for equivalent parallel plate. (Upper row) 0.2 MPa, (middle row) 2 MPa, (lower row) 20 MPa, (Left column) JRC = 4, (right column) JRC = 10.

Table 7
Selected percentiles of specific flow wetted surface CDFs in Figs. 13 and 14 together with the values from the parallel plate equivalent.

σ	JRC	∇	1 %	10 %	50 %	90 %	*99 %*[*]	parallel
0.2	4	X	$4.16\cdot10^{3}$	$4.19\cdot10^{3}$	$4.24\cdot10^{3}$	$4.30\cdot10^{3}$	$4.35\cdot10^{3}$	$4.72\cdot10^{3}$
0.2	10	X	$3.12\cdot10^{3}$	$3.20\cdot10^{3}$	$3.35\cdot10^{3}$	$3.61\cdot10^{3}$	$4.55\cdot10^{3}$	$4.06\cdot10^{3}$
2	4	X	$5.42\cdot10^{3}$	$5.48\cdot10^{3}$	$5.59\cdot10^{3}$	$5.73\cdot10^{3}$	$5.97\cdot10^{3}$	$6.36\cdot10^{3}$
2	10	X	$4.08\cdot10^{3}$	$4.24\cdot10^{3}$	$4.63\cdot10^{3}$	$6.17\cdot10^{3}$	$8.77\cdot10^{4}$	$6.18\cdot10^{3}$
20	4	X	$1.47\cdot10^{4}$	$1.82\cdot10^{4}$	$4.68\cdot10^{4}$	$5.91\cdot10^{5}$	$8.75\cdot10^{6}$	$2.44\cdot10^{4}$
20	10	X	$6.68\cdot10^{3}$	$7.60\cdot10^{3}$	$1.41\cdot10^{4}$	$1.86\cdot10^{5}$	$2.86\cdot10^{6}$	$2.07\cdot10^{4}$
0.2	4	Y	$3.92\cdot10^{3}$	$4.04\cdot10^{3}$	$4.24\cdot10^{3}$	$4.46\cdot10^{3}$	$4.66\cdot10^{3}$	$4.51\cdot10^{3}$
0.2	10	Y	$2.78\cdot10^{3}$	$2.93\cdot10^{3}$	$3.27\cdot10^{3}$	$3.86\cdot10^{3}$	$4.98\cdot10^{3}$	$3.57\cdot10^{3}$
2	4	Y	$5.03\cdot10^{3}$	$5.24\cdot10^{3}$	$5.58\cdot10^{3}$	$6.03\cdot10^{3}$	$6.60\cdot10^{3}$	$5.89\cdot10^{3}$
2	10	Y	$3.54\cdot10^{3}$	$3.80\cdot10^{3}$	$4.43\cdot10^{3}$	$6.04\cdot10^{3}$	$4.67\cdot10^{4}$	$4.88\cdot10^{3}$
20	4	Y	$1.22\cdot10^{4}$	$1.46\cdot10^{4}$	$2.94\cdot10^{4}$	$3.96\cdot10^{5}$	$5.82\cdot10^{6}$	$1.64\cdot10^{4}$
20	10	Y	$5.55\cdot10^{3}$	$6.25\cdot10^{3}$	$9.24\cdot10^{3}$	$8.84\cdot10^{4}$	$1.87\cdot10^{6}$	$1.07\cdot10^{4}$

[*] Observe that the values from the 99th percentile might be biased due to small numerical errors

For the case where the global head gradient is parallel to the shear direction the median specific flow wetted surface increases by increased normal stress, Fig. 13 (a *vs* e, b *vs* f) and Table 7. The increase is between 4 and 11 times where the smoother fractures have the largest increase. As the roughness is increased the median specific flow wetted surface will decrease, Fig. 13 (a *vs* b, c *vs* d, e *vs* f) and Table 7. The decrease is 1.2–3 times where the fractures subjected to the largest normal stress have the largest decrease when the roughness is changed. The same pattern is seen for the fastest particles but to a less extent. For the slowest particles the specific flow wetted surface increases almost 3 orders of magnitude when the normal stress is increased from 0.2 MPa to 20 MPa. The change in specific flow wetted surface due to change in initial roughness follow the same pattern as for the transport resistance, i.e. the rougher fractures have less transport resistance for fast and moderate particles, but a larger specific flow wetted surface for the slower particles, except for the 20 MPa case.

For the case where the global head gradient is perpendicular to the shear direction the median specific flow wetted surface increase 3–7 times when stress is increased; the smoother the fracture the larger the increase, Fig. (14 a *vs* e, b *vs* f) and Table 7. The decrease in specific flow wetted surface due to increased roughness is between 1.3 and 3 times, where the largest decrease is related to the highest normal stress. For the fastest particles the corresponding numbers are 2–3 times when stress is increased and 1.5–2 times as JRC is decreased. The slowest particles, once again, show an ambiguous behaviour where the specific flow wetted surface increases with increased JRC for low stresses, but increase for 20 MPa. Hence, there is a clear increase in specific flow wetted surface as the normal stress increases and a somewhat decrease as roughness increase, except for the very slow particles.

The increase in specific flow wetted surface due to increased normal stress is expected since the aperture distribution shifts the median towards smaller apertures when normal stress is increased, see Fig. 4. It is also natural that the median specific flow wetted surface decreases as the initial roughness increases, since the mean of the aperture distribution increases, as well as the variance. However, the specific flow wetted surface is larger for the rougher fractures under lower normal stress (0.2 and 2.0 MPa). This behaviour of ca 1 % slowest particles is not fully understood, but it may be an effect of numerical errors.

The equivalent parallel plate approach severely overestimates the specific flow wetted surface, (i.e. the probability for solutes to interact with the fracture surface) especially when the global gradient is aligned with the shear direction; the normal stress is low; and the roughness large. This is explained by the flow paths converging towards channels with large aperture and high conductivity. Hence the factor $1/b$ in Eq. 15 becomes smaller for the elements visited by the flow paths than the average $1/b$ of the equivalent parallel plate.

5. Discussion

The model for shearing synthetic fractures is simple, but it seems to well capture the overall behaviour of real fractures (Casagrande et al., 2018; Stigsson and Johansson, 2019, in Stigsson, 2019). Also, the flow solver is simple, using triangular linear 2D finite elements for solving Reynolds lubrication equation. The advantage of using these two models, though, is that rather large problems might be solved using standard computers and that it is possible to run several Monte Carlo realisations of each fracture within reasonable time frames. Despite the release of more than one million particles for each parameter combination, the variance did not become stable above the 99th percentile for some combinations, due to long tails in the distributions. The long tails might be a result of the generated fractures being fractal which affects the aperture distribution and correlation structure when sheared. It may also have been affected by the small numerical error that the Galerkin FE scheme introduces when solving the head field. Hence, one should be cautious in drawing conclusions from results at the very tail (above 99th percentile). The aperture field that arises from the shearing of the fractal surfaces will consist of areas with large apertures on the leeside of the shear direction and areas of contact or small apertures on the push side. Those areas will be elongated perpendicular to the shear direction and, hence, generate high conductive channels perpendicular to shear direction surrounded by low conductive areas. This correlation structure will generate relatively straight and fast pathways for flow and particles when the global head gradient is perpendicular to the shear direction. When the global head gradient is parallel to the shear direction the areas of low conductance will force the flow and particles to follow these channels perpendicular to global head gradient to find the paths of least resistance to bypass.

The trends in the results are usually consistent, (e.g. increased difference in evaluated parameter by increased property) for the low percentiles up to about the 90th percentile. Above that percentile, there is sometimes a reverse behaviour (e.g. decreased difference in evaluated parameter by increased property). This may be an effect of the long tails of the distributions or the small errors in mass balance for the finite element scheme. Hence, the results should be omitted from analyses.

Analysing the coherent results from the percentiles below the 90th percentile shows that increased normal stress results in longer travel times, longer travel paths, higher transport resistance and larger specific flow wetted surface. This is expected since a higher normal load will decrease the aperture, Fig. 4. A smaller aperture yields smaller transmissivity (Eq. 7) and thereby smaller velocity which extends the time it takes for a particle to travel through the fracture. Larger normal stress will also increase the areas in contact and hence force the flow around these obstacles resulting in longer travel paths. As both the aperture and velocity decrease with increased normal stress the denominator in Eq. 13 becomes smaller and hence the quotient larger for a constant element length. This together with more elements visited by the particles, Eq. 14, will naturally increase the transport resistance when the normal stress is increased. The specific flow wetted surface mainly reflects the area that a volume of water may interact with along a flow path. As the aperture decreases the volume of water between the bounding surfaces decreases as well, which leads to a larger specific flow wetted surface if the travel time is constant, Eq. 16. The travel time is not constant, but increases with increased normal stress, and hence, counteracts the effect of larger transport resistance. However, the transport resistance in the numerator increases faster than the travel time in the denominator and hence the specific flow wetted surface increases as the normal stress increases.

Increased initial roughness results in shorter travel times, longer travel paths, lower transport resistance and smaller specific flow wetted surface, analysing the coherent results below the 90th percentile. The increased travel length, due to increased initial roughness, is an effect of the rougher fracture having larger Hurst exponent and thereby stronger correlation for the asperity distribution, i.e. larger areas with similar topography will emerge. As the areas of low conductance increase the travel path to bypass them will hence be longer. However, the same effect will also yield for the channels of high conductance that will become more persistent. These persistent channels, though longer, will be more transmissive and hence the travel times will be smaller as the roughness increases. The explanation to the transport resistance decreasing with increased roughness also relies on the development of persistent channels on the leeside of the fracture surface's ridges, i.e. the rougher fractures have larger probability of developing paths with more persistent large apertures. The decrease in specific flow wetted surface is an effect of the rough fractures having more elements of large aperture attracting the flow.

The results from the investigated high-resolution fractures may be used to map properties to flow and transport models using a channel network approach, such as models by Dessirier (2023) and Zou et al. (2023). By such approach the channels may get probabilistic properties from high resolution studies such as the one presented here. However, first the results need to be confirmed using real fractures at different scales. Also, the method developed by Casagrande et al. (2018) could be evolved to consider constant normal stiffness conditions to reflect the stress situation deep in the rock mass. Thereafter, more comprehensive studies using other fractal parameters for the fractures need to be considered. Another issue that needs to be solved is the behaviour of the intersections of fractures, i.e. if, and to what extent, the intersections allow for correlation of aperture between intersecting fractures.

6. Conclusions

Generating realistic fractures using fractal theories in combination with numerical shearing, flow and transport behaviour of rough fractures can be studied under different normal stress and different initial roughness. In this study, laminar flow through sheared synthetic fractures with JRC, in the range 4–10, are studied under normal stress between 0.2 and 20 MPa. The methods used here include the generation of fractures, shearing the fractures, calculating the aperture field, solving the flow field and tracking particles through the fractures. The main conclusion is that the shearing of the fractures will result in spatial aperture correlation structures that might be difficult to generate using geostatistical methods. Other conclusions are that an increase in normal stress will generally result in longer travel times, longer travel paths, higher transport resistance and larger specific flow wetted surface while an increase in initial roughness will generally result in shorter travel times, longer travel paths, lower transport resistance and smaller specific flow wetted surface. These effects will be more pronounced when the global head gradient is aligned with the shear direction compared to the direction transverse to it. The study also shows that using parallel plate will often be too optimistic, i.e. non-conservative, compared to the fastest particles and sometimes even too optimistic compared to the value of 50th percentile particle.

CRediT authorship contribution statement

Martin Stigsson: Writing – original draft, Visualization, Software, Project administration, Methodology, Investigation, Formal analysis, Data curation, Conceptualization. **Diego Mas Ivars:** Writing – review & editing, Conceptualization. **Jan-Olof Selroos:** Writing – review & editing. **Vladimir Cvetkovic:** Writing – review & editing.

Declaration of Competing Interest

The authors declare the following financial interests/personal relationships which may be considered as potential competing interests: Martin Stigsson is currently employed by Swedish Nuclear Fuel and Waste Management Co. If there are other authors, they declare that they have no known competing financial interests or personal relationships that could have appeared to influence the work reported in this paper.

References

Golder Associates, 2001. MAFIC – Matrix/Fracture Interaction Code with Heat and Solute Transport. User Documentation. Version 2.0 Golder Associates Inc. Redmond, Washington.

Barton, N., 1973. Review of a new shear-strength criterion for rock joints. Eng. Geol. 7 (4), 287–332. https://doi.org/10.1016/0013-7952(73)90013-6

Blessent, D., Therrien, R., Gable, C.W., 2011. Large-scale numerical simulation of groundwater flow and solute transport in discretely-fractured crystalline bedrock. Adv. Water Resour. 34, 1539–1552. https://doi.org/10.1016/j.advwatres.2011.09.008

Brodsky, E., Gilchrist, J., Sagy, A., Collettini, C., 2011. Faults smooth gradually as a function of slip. Earth Planet. Sci. Lett. 302, 185–193.

Brown, S.R., 1987. A note on the description of surface roughness using fractal dimension. Geophys. Res. Lett. 14, 1095–1098.

Brush, D.J., Thomson, N.R., 2003. Fluid flow in synthetic rough-walled fractures: Navier-Stokes, stokes, and local cubic law simulations. Water Resour. Res. 39 (4), 1085. https://doi.org/10.1029/2002WR001346

Candela, T., Renard, F., Bouchon, M., Marsan, D., Schmittbuhl, J., Voisin, C., 2009. Characterization of fault roughness at various scales: implications of three-dimensional high resolution topography measurement. Pure Appl. Geophys 166 (10), 1817–1851.

Candela, T., Renard, F., Klinger, Y., Mair, K., Schmittbuhl, J., Brodsky, E., 2012. Roughness of fault surfaces over nine decades of length scales. J. Geophys. Res. 117, B08409. https://doi.org/10.1029/2011JB009041

Casagrande, D., Buzzi, O., Giacomini, A., Lambert, C., Fenton, G., 2018. A new stochastic approach to predict peak and residual shear strength of natural rock discontinuities. Rock. Mech. Rock. Eng. 51, 69–99. https://doi.org/10.1007/s00603-017-1302-3

Cvetkovic, V., Frampton, A., 2010. Transport and retention from single to multiple fractures in crystalline rock at Äspö (Sweden): 2. Fracture network simulations and generic retention model. Water Resour. Res. 46, W05506. https://doi.org/10.1029/2009WR008030

Cvetkovic, V., Frampton, A., 2012. Solute transport and retention in three-dimensional fracture networks. Water Resour. Res. 48, W02509. https://doi.org/10.1029/2011WR011086

Cvetkovic, V., Gotovac, H., 2013. Flow-dependence of matrix diffusion in highly heterogeneous rock fractures. Water Resour. Res. 49, 7587–7597.

Cvetkovic, V., Painter, S., Outters, N., Selroos, J.O., 2004. Stochastic simulation of radionuclide migration in discretely fractured rock near the Äspö hard rock laboratory. Water Resour. Res. 40, W02404. https://doi.org/10.1029/2003WR002655

Cvetkovic, V., Selroos, J.O., Cheng, H., 1999. Transport of reactive tracers in rock fractures. J. Fluid Mech. 378, 335–356.

Dagan, G., Cvetkovic, V., Shapiro, A., 1992. A solute flux approach to transport in heterogeneous formations: 1. The general framework. Water Resour. Res. 28 (5), 1369–1376.

Den Outer, A., Kaashoek, J., Hack, H., 1995. Difficulties with using continuous fractal theory for discontinuity surfaces. Int. J. Rock. Mech. Min. Sci. Geomech. Abstr. 32 (1), 3–9. https://doi.org/10.1016/0148-9062(94)00025-X

Dessirier, B., 2023. bende937/pychan3d: Pychan3d_orig (v1.0.0) [Software]. Zenodo. https://doi.org/10.5281/zenodo.7799216

Dessirier, B., Tsang, C.F., Niemi, A., 2018. A new scripting library for modeling flow and transport in fractured rock with channel networks. Comput. Geosci. 111, 181–189. https://doi.org/10.1016/j.cageo.2017.11.013

Frampton, A., 2025a. Flow channelling and variability in transit times and tortuosity in a fractured rock model with small scale heterogeneity. Adv. Geosci. 65, 149–158. https://doi.org/10.5194/adgeo-65-149-2025

Frampton A., 2025b. Enhanced transport with early arrivals and reduced attenuation for ensemble realisations of discrete fracture networks with internal fracture heterogeneity. Hydrogeology Journal. Accepted.

Frampton, A., Cvetkovic, V., 2011. Numerical and analytical modeling of advective travel times in realistic three-dimensional fracture networks. Water Resour. Res. 47, 2010WR009290. https://doi.org/10.1029/2010WR009290

Frampton A., Hyman J.D., Zou L., 2018. Advective transport in a synthetic discrete fracture system with internal variability in permeability. In: Proceedings of the 2nd International Discrete Fracture Network Engineering Conference, 20-22 June, Seattle, Washington, USA. ARMA DFNE 18–0932.

Frampton, A., Hyman, J.D., Zou, L., 2019. Advective transport in discrete fracture networks with connected and disconnected textures representing internal aperture variability. Water Resour. Res. 55 (7), 5487–5501.

Gallant, J.C., Moore, I.D., Hutchinson, M.F., Gessler, P., 1994. Estimating fractal dimension of profiles: a comparison of methods. Math. Geol. 26, 455–481. https://doi.org/10.1007/BF02083489

Glamheden R, Curtis P, 2006. Comparative evaluation of core mapping results for KFM06C and KLX07B. Svensk Kärnbränslehantering AB. Available at: http://www.skb.se/upload/publications/pdf/R-06-55.pdf.

Gustafson G., 2012. Hydrogeology for Rock Engineers. BeFo, Stockholm.

Gylling, B., Moreno, L., Neretnieks, I., 1999. The channel network model – a tool for transport simulations in fractured media. Groundwater 37 (3), 367–375 https://doi-org.focus.lib.kth.se/10.1111/j.1745-6584.1999.tb01113.x.

Hartley L., Appleyard P., Baxter S., Hoek J., Roberts D., Swan D., 2012. Development of a Hydrogeological Discrete Fracture Network Model for the Olkiluoto Site Descriptive Model 2011. WR 12–32. POSIVA OY.

Hartley L., Appleyard P., Baxter S., Hoek J., Joyce S., Mosley K., Williams T., Fox A., Cottrell M., La Pointe P., Gehör S., Darcel C., Le Goc R., Aaltonen I., Vanhanarkaus O., Löfman J., Poteri A., 2017. Discrete Fracture Network Modelling (Version 3) in Support of Olkiluoto Site Description 2018. WR 17–32. POSIVA OY.

Hong-fa, X., Yan-ru, L., Xin-yu, L., Tieping, L., 2002. Fractal simulation of joint profiles and relationship between JRC and fractal dimension. Chin. J. Rock. Mech. Eng. 21 (11), 1663–1666.

Hurst, H., 1957. A suggested statistical model of some time series which occur in nature. Nature 180, 494.

Hyman, J.D., 2020. Flow channeling in fracture networks: characterizing the effect of density on preferential flow path formation. Water Resour. Res. 56 (9). https://doi.org/10.1029/2020WR027986

Itasca, 2013. 3DEC - Three dimensional distinct element code, Version 5.0. Minneapolis: Itasca Consulting Group Inc.

Itasca, 2014a. PFC, Particle Flow Code, Version 5.0. Minneapolis: Itasca Consulting Group Inc.

Itasca, 2014b. UDEC - Universal Distinct Element Code, Version 6.0. Minneapolis: Itasca Consulting Group Inc.

Johansson, F., Stille, H., 2014. A conceptual model for the peak shear strength of fresh and unweathered rock joints. Int. J. Rock. Mech. Min. Sci. 69, 31–38.

Koyama, T., Fardin, N., Jing, L., Stephansson, O., 2006. Numerical simulation of shear-induced flow anisotropy and scale-dependent aperture and transmissivity evolution of rock fracture replicas. Int. J. Rock. Mech. Min. Sci. 43, 89–106.

Lee, H.-S., Ahn, K.-W., 2004. A prototype of digital photogrammetric algorithm for estimating roughness of rock surface. Geosci. J. 8 (3), 333–341.

Maillot, J., Davy, P., le Goc, R., Darcel, C., de Dreuzy, J.R., 2016. Connectivity, permeability, and channeling in randomly distributed and kinematically defined discrete fracture network models. Water Resour. Res. 52, 8526–8545. https://doi.org/10.1002/2016WR018973

Makedonska, N., Hyman, J.D., Karra, S., Painter, S.L., Gable, C.W., Viswanathan, H.S., 2016. Evaluating the effect of internal aperture variability on transport in kilometer scale discrete fracture networks. Adv. Water Resour. 94, 486–497. https://doi.org/10.1016/j.advwatres.2016.06.010

Malinverno, A., 1990. A simple method to estimate the fractal dimension of a self affine series. Geophys Res Lett. 17, 1953–1956.

Mandelbrot, B.B., 1985. Self-Affine fractals and fractal dimension. Phys. Scr. 32, 257–260.

Mattila, J., Viola, G., 2014. New constraints on 1.7 gyr of brittle tectonic evolution in southwestern Finland derived from a structural study at the site of a potential nuclear waste repository (Olkiluoto Island). J. Struct. Geol. 67, 50–74.

Moreno, L., Neretnieks, I., 1993. Flow and nuclide transport in fractured media: the importance of the flow-wetted surface for radionuclide migration. J. Contam. Hydrol. 13, 49–71.

Munier, R., Talbot, C.J., 1993. Segmentation, fragmentation and jostling of cratonic basement in and near asp € o, southeast Sweden. Tectonics 12, 713–727.

Neuman, S.P., 2005. Trends, prospects and challenges in quantifying flow and transport through fractured rocks. Hydrogeol. J. 13 (1), 124–147.

Odling, N.E., 1994. Natural fracture profiles, fractal dimension and joint roughness coefficients. Rock. Mech. Rock. Eng. 27 (3), 135–153.

Ogilvie, S.R., Isakov, E., Glover, P.W.J., 2006. Fluid flow through rough fractures in rocks. Ii: a new matching model for rough rock fractures. Earth Planet. Sci. Lett. 241, 454–465.

Oron, A.P., Berkowitz, B., 1998. Flow in rock fractures: the local cubic law assumption Re-examined. Water Resour. Res. 34, 2811–2815.

Renard, F., Voisin, C., Marsan, D., Schmitbuhl, J., 2006. High resolution 3D laser scanner measurements of a strike-slip fault quantify its morphological anisotropy at all scales. Geophys. Res. Lett. 33, L04305. https://doi.org/10.1029/2005GL025038

Russ J., 1994. Fractal Surfaces. Plenum Press, New York. ISBN 0-306-44702-9.

Saintot, A., Stephens, M.B., Viola, G., Nordgulen, Ø., 2011. Brittle tectonic evolution and paleostress field reconstruction in the southwestern part of the fennoscandian shield, forsmark, Sweden. Tectonics 30, TC4002.

Saupe D., 1988. The Science of Fractal Images. Springer-Verlag New York, Inc. New York, NY, USA ©1988. ISBN:0-387-96608-0.

Scheiber, T., Viola, G., 2018. Complex bedrock fracture patterns: a multipronged approach to resolve their evolution in space and time. Tectonics 37 (4), 1030–1062.

SKB, 2008. Site description of Forsmark at completion of the site investigation phase. SDM-Site Forsmark. SKB TR-08-05, Svensk Kärnbränslehantering AB. Available at: 〈https://www.skb.se/publikation/1868223/TR-08-05.pdf〉.

Stigsson M., 2015. Parameterization of fractures—methods and evaluation of fractal fracture surfaces. W*R* 15–27. POSIVA OY.

Stigsson M., (2019). Structural Uncertainties of Rock Fractures and their Effect on Flow and Tracer Transport. PhD Thesis, TRITA-ABE-DLT-1927.

Stigsson M., Johansson F., 2019. Some aspects on the applicability of peak shear strength criteria. Manuscript in progress in Stigsson (2019).

Stigsson, M., Mas Ivars, D., 2018. A novel conceptual approach to objectively determine JRC using fractal dimension and asperity distribution of mapped fracture traces. Rock. Mech. Rock. Eng. 52, 1041–1054. https://doi.org/10.1007/s00603-018-1651-6

Stock B., Frampton A., 2022. Processing and Conversion of Raw Point-Cloud Laser Measurements and Auxiliary Data of Rough-Surfaced Fractures To Generate Corresponding Fracture Aperture Fields. Presented at the 3rd International Discrete Fracture Network Engineering Conference, OnePetro, Santa Fe, New Mexico, USA. https://doi.org/10.56952/ARMA-DFNE-22-0020.

Stock, B., Frampton, A., 2025a. Analysis and generation of Rough-Surfaced fractures with variable aperture based on Self-Affine methods using surface scan measurements. Rock. Mech. Rock. Eng. 58, 4827–4848. https://doi.org/10.1007/s00603-024-04381-9

Stock B., Frampton A., 2025b. Upscaling fracture aperture fields using self-affine methods with evaluation against laboratory flow measurements. 59th U.S. Rock Mechanics/Geomechanics Symposium, Santa Fe, New Mexico, June 2025. Paper Number: ARMA-2025-0681. https://doi.org/10.56952/ARMA-2025-0681.

Thörn, J., Fransson, Å., 2015. A new apparatus and methodology for hydromechanical testing and geometry scanning of a rock fracture under low normal stress. Int. J. Rock. Mech. Min. Sci. 79, 216–226. https://doi.org/10.1016/j.ijrmms.2015.08.015

Trinchero, P., Zou, L., de La Iglesia, M., Iraola, A., Bruines, P., Deissmann, G., 2024. Experimental and numerical analysis of flow through a natural rough fracture subject to normal loading. Sci. Rep. 14, 5587. https://doi.org/10.1038/s41598-024-55751-w

Tsang, C.-F., Neretnieks, I., Tsang, Y., 2015. Hydrologic issues associated with nuclear waste repositories. Water Resour. Res. 51, 6923–6972. https://doi.org/10.1002/2015WR017641

Viola G., Venvik Ganerød G., Wahlgren C.-H., 2009. Unravelling 1.5 Gyr of brittle deformation history in the Laxemar-Simpevarp area, SE Sweden: a contribution to the Swedish site investigation study for the disposal of highly radioactive nuclear waste. Tectonics 28. TC5007.

Wang, L., Cardenas, M.B., Slottke, D.T., Ketcham, R.A., Sharp, J.M., 2015. Modification of the local cubic law of fracture flow for weak inertia, tortuosity, and roughness. Water Resour. Res. 51, 2064–2080. https://doi.org/10.1002/2014WR015815

Wels, C., Smith, L., Vandergraaf, T.T., 1996. Influence of specific surface area on transport of sorbing solutes in fractures: an experimental analysis. Water Res. Res. 32 (7), 1943–1954.

Witherspoon, P.A., Wang, J.S.Y., Iwai, K., Gale, J.E., 1980. Validity of cubic law for fluid flow in a deformable rock fracture". Water Res. Res. 16 (61), 1016–1024.

Yeo, I.W., Ge, S., 2005. Applicable range of the reynolds equation for fluid flow in a rock fracture. Geosci. J. 9 (4), 347–352.

Zimmerman R.W., Bodvarsson G.S., 1994. Hydraulic Conductivity of Rock Fractures. Earth Sciences Division, Lawrence Berkeley Laboratory, University of California, Berkeley, CA 94720.

Zimmerman, R.W., Bodvarsson, G.S., 1996. Hydraulic conductivity of rock fractures. Transp. Porous Media 23, 1–30.

Zou, L., Jing, L., Cvetkovic, V., 2015. Roughness decomposition and nonlinear fluid flow in a single rock fracture. Int. J. Rock. Mech. Min. Sci. 75 (2015), 102–118. https://doi.org/10.1016/j.ijrmms.2015.01.016

Zou, L., Jing, L., Cvetkovic, V., 2017a. Shear-enhanced nonlinear flow in rough-walled rock fractures. Int. J. Rock. Mech. Min. Sci. 97 (2017), 33–45.

Zou, L., Jing, L., Cvetkovic, V., 2017b. Modeling of flow and mixing in 3D rough-walled rock fracture intersections. Adv. Water Resour. 107, 1–9.

Zou, L., Selroos, J.-O., Poteri, A., Cvetkovic, V., 2023. Parameterization of a channel network model for groundwater flow in crystalline rock using geological and hydraulic test data. May 2023. Eng. Geol. 317, 107060. https://doi.org/10.1016/j.enggeo.2023.107060